UAM Icing: Ice Accretion Experiments and CFD Icing Simulations on Rotors for eVTOL Unmanned Aircraft

Henidya Hermawaran, Nicolas C. Müller
Department of Technical Cybernetics, NTNU, Trondheim, Norway

Thorsten Lutz
IAG, University of Stuttgart, Stuttgart, Germany

Richard Hann
Department of Technical Cybernetics, NTNU, Trondheim, Norway

Abstract

Urban air mobility (UAM) is a fast-growing industry that utilizes electric vertical take-off and landing (eVTOL) technologies to operate in densely populated urban areas with limited space. However, atmospheric icing serves as a limitation to its operational envelope as in-flight icing can happen all year round anywhere around the globe. Since icing in smaller aviation systems is still an emerging topic, there is a necessity to study icing of eVTOL rotors specifically. Two rotor geometries were chosen for this study. A small 15-inch rotor was selected to illustrate a multirotor UAV drone, while a large 80-inch rotor was chosen to represent a UAM passenger aircraft. The ice accretion experiments were conducted in an icing wind tunnel on the small 15-inch rotor. The icing simulations were performed using FENSAP-ICE. The ice accretion simulations of the 15-inch rotor sections at −5 °C show a large, rather streamlined ice shape instead of the expected glaze ice characteristics. At −15 °C the numerical ice accretion presents the typical rime ice shape. The results of the 80-inch rotor simulation present more varied ice shapes, which could indicate higher sensitivity towards the icing condition. Ice horns formed at temperatures close to freezing and the flow separation aft of the ice led to significant aerodynamic penalties. The 3D ice accretion simulation of the 80-inch rotor shows discrepancies with the 2D results as it does not predict ice accretion at the outer region of the blades at − 15 °C. This could be due to the higher stagnation temperature, increased friction, and three-dimensional crossflows preventing ice accumulation. The performance degradation simulations show that ice accretion causes significant aerodynamic penalties, especially in cases where horn ice accretion forms. Finally, the anti-icing loads required to mitigate ice accretion thermally were calculated. Both rotors require high power consumption for a fully evaporative IPS design.

Introduction

One of the efforts to make future transportation of passengers and goods fossil-fuel-free, reliable, and time-efficient is by utilizing air space with means of advanced air mobility (AAM). A subgroup of the AAM concept is urban air mobility (UAM) which concentrates on applications in urban and metropolitan areas, whereas the AAM concept includes inter-city applications [1, 2]. This new air transportation system is made possible by electric vertical take-off and landing (eVTOL) aircraft which can operate in densely populated areas. Electric VTOL aircraft come in various shapes, sizes, and configurations as their design is mostly dictated by their intended application. In the sense of an AAM ecosystem, a small eVTOL's mail application would be cargo delivery while a large eVTOL focuses on passenger transport, but not exclusively. To date, most commercial UAVs operate within visual line of sight with rotary wings [3]. However, there has been increased interest in UAV applications beyond the visual line of sight and either fully autonomous or remotely piloted. Currently, most UAM aircraft designs introduced to the public are configured with a pilot on board. However, the long-term goal of most UAM service providers is to implement autonomous UAM aircraft to push down operational costs [4]. The UAM industry is projected to grow fast. A market study by Booz Allen Hamilton [5] commissioned by NASA predicted a market value of USD 500 billion for an unconstrained long-term market. This rapid-growing industry is, however, confronted with operational hurdles. One of them being atmospheric in-flight icing.

In-flight icing is a phenomenon that happens when supercooled water droplets exist in the air and upon collision can cause ice formation on an aircraft. The shape and size of the ice accretion depend on the vehicle parameters, such as the size of the airframe and airspeed velocity, and the meteorological parameters, for example, liquid water content (LWC) and droplet size [3]. The Federal Aviation Regulations published documentation [6] concerning the definition of icing conditions to aid in the development of ice mitigation systems and for aircraft certification purposes. Previous studies show that icing conditions can exist any time of the year and anywhere around the globe [7, 8]. This imposes a significant restriction on an aircraft's availability as current regulations forbid operations in known icing conditions [9].

The icing process is divided into two steps: the droplet impingement and the freezing process [10]. To determine the impingement, the droplet trajectory must first be calculated. Small droplets tend to follow the airflow direction, while larger droplets are more likely to collide. This is owed to the droplet trajectory physics, which is determined by the balance between the droplet inertia and the aerodynamic forces acting on the droplet. Furthermore, the size and form of an airfoil influence the degree to which the aerodynamic force on the airfoil can deflect the droplets. Small and thin airfoils have less impact on the flow field and therefore generate weaker aerodynamic forces compared to larger and thicker airfoils. As a result, small airfoils have higher collision efficiency than large airfoils [11]. After impingement, there is a freezing process which is defined by the thermal conduction between the airfoil surface and the impinging water as well as the heat transfer to the air. Icing increases the surface roughness of an airfoil, which influences the convective heat transfer and eventually lowers the surface temperature further [10].

It is also important to note that the water freezing duration plays a role in the final ice shape. Droplets that freeze immediately upon impact will have a different shape compared to droplets that do not. There are three commonly observed icing types: rime, glaze, and mixed ice.

Rime ice is characterized by its opaque white color which comes from trapped air between the frozen water droplets. Typically, rime ice has a streamlined shape and the separation bubble aft of the ice is small. Therefore, the aerodynamic penalties are less severe [12]. Rime ice occurs in low temperatures where the impinging droplets freeze immediately upon collision. When the droplets do not immediately freeze, a thin water film is formed on the airfoil surface. This water film would either gradually freeze, which is called glaze ice, or run back in the chord direction. Glaze ice typically occurs at temperatures near the freezing point. Glaze ice leads to strong aerodynamic penalties [12], as the ice shape evolves irregularly and can develop ice horns, which cause large flow separation regions. Glaze ice appears clear as it does not contain trapped air. A combination of the two ice types is called mixed ice. As the ice formation depends on several parameters that often fluctuate within a short period, the ice shapes obtained in real life often contain characteristics of both rime and glaze ice. Mixed ice shape forms in a variety of shapes and it often causes more severe aerodynamic performance degradations [13]. Various wind tunnel experiments, flight tests, and numerical simulations [14] have shown, that ice formation leads to performance penalties. A study on the performance of UAV wing airfoils in various icing conditions concluded that in the worst case at an icing temperature of −2 °C and an MVD of 20 µm, the ice accretion reduced the lift by 35% while drag is increased up to 400% [15]. Lynch and Khodadoust [16] and Bragg et al. [12] have provided an extensive study on the effects of ice accretion on aircraft aerodynamics and the flow physics.

The problem with icing affects all aircraft regardless of size and configuration. A notable amount of research on the consequences of icing on larger manned aircraft systems has been conducted over the years [16–18]. While icing in manned aviation is considered well-established, the topic of icing on unmanned and other newer configurations is an emerging topic that still lacks comprehensive understanding. The topic of UAV icing wasn't addressed earlier due to the nature of early UAV applications being almost exclusively for military operations in hot humid environments [3]. Several differences exist between the icing behavior in manned aviation and smaller aviation vehicles. This is due to the size and flight velocity difference, which consequently influences the flow regime. Larger manned aircraft typically operate at higher Reynolds numbers ($\mathrm{Re} = 10^7 - 10^9$), whereas UAVs and smaller aircraft feature smaller Reynold numbers ($\mathrm{Re} = 10^5 - 10^7$) [19]. This difference heavily influences the ice accretion process [20]. Furthermore, there are notable challenges in computational fluid dynamic (CFD) icing studies for aircraft in the lower Reynolds number regime [21]. Another difference between icing in larger and smaller aircraft is the flight velocity. Larger aircraft typically cruise with higher velocities. This leads to stronger aerodynamic heating caused by viscous friction, which is often enough to counteract ice build-up at temperatures close to the freezing point. The aerodynamic heating of aircraft with slower velocities is often so low that it is negligible [3].

In the last ten years, there has been more research work done on UAV icing [15, 22, 23]. However, there is still a lack of studies on eVTOL drones and UAM aircraft rotors specifically. Previous research has shown that rotating lifting surfaces, such as rotors and propellers, are more sensitive to icing compared to fixed-wing [3]. This is owed to the higher relative airspeed at the tips of the blade and the smaller chord length and leading-edge radius [11]. Another study on UAV propellers shows a significant thrust reduction and power increase after a 100-second exposure to moderate icing conditions [24]. Research on a UAV rotor blade exhibits similar performance degradation [25]. Furthermore, the effect of centrifugal forces can lead to ice shedding, which increases rotor imbalances [26]. With the before-mentioned aspects in consideration, closing this gap of knowledge is seen as a necessity. At the time of writing, there is no known mature ice mitigation system available for UAVs and UAM aircraft. To increase the availability, reliability, and safety of an eVTOL aircraft, the rotor icing challenges must be addressed. This paper aims to provide a first insight into the ice accretion on eVTOL rotors and the corresponding performance reduction and also to assess the required anti-icing loads necessary to mitigate the problem.

Methods

Ice Accretion Experiments

In this study, an ice accretion experimental campaign was conducted on a 15-inch two-bladed rotor at the VTT Technical Research Center icing wind tunnel [27] in Finland. The wind tunnel is an open loop system with a closed test section. The wind tunnel is placed inside a cold chamber which has a temperature range from +25 °C to −25 °C. The spray nozzles inside the wind tunnel inject liquid water into the airflow. The liquid water content inside the facility can be set between 0.1 g/m^3 to 1 g/m^3 with a median volume diameter of 12 µm to 30 µm. The liquid water content was calibrated at a wind speed of 25 m/s using a rotating cylinder. The water flow rate was kept constant so that the LWC at the test velocities can be calculated by the proportions of the wind speeds.

The rotor was mounted on a Series 1580 Test Stand by Tyto Robotics [28] which can record the thrust up to 5 kgF, the torque up to 2 Nm, and with an optical RPM probe the rotation rate of the rotor up to 30,000 RPM. This test stand was calibrated with known forces before the start of the experiments. Weight was utilized to calibrate the thrust and offset weight for the torque. The rotor was controlled by a JavaScript script inside Tyto Robotics software environment. This uses a PI controller to keep the rotation rate of the rotor constant during the experiments. A Phantom VEO 710L high-speed camera was used to record the ice accretion process. A laser was shown through the rotation plane of the rotor and a photodiode measured the strength of the signal. An Arduino Unio WiFi REV2 was used to transform the signal into a digital output which is then used to synchronize the high-speed camera with the rotation of the rotor. Two multi-LED QT lights were used to illuminate the rotor for the high-speed camera. They are also synchronized with the rotation of the rotor. This reduces the impact of the strong lights on the ice accretion on the rotors. The ice shapes were recorded by means of photogrammetry. The setup used a Foldio 3 photo studio with a turntable. The images were captured using a SONY Alpha A6400 with an 18-50 mm objective lens. The rotor was mounted on a holder on the turntable, where 48 images were taken in an orbit. The images were then analyzed with the software Agisoft Metashape. Furthermore, the images were turned into a mesh which could then be imported into CAD software to extract the ice shape. This process was then performed for each existing ice shape.

The ice accretion experiments were conducted at three different temperatures: − 5 °C, − 10 °C, and − 15 °C. The LWC and MVD of the droplets during the experiments were set to 0.41 g/m^3 and 24.3 µm, respectively. The rotation rate of the rotor is 5000 RPM. A short icing duration of 60 s was chosen to consider the ice build-up before shedding occurs. It should be highlighted, that there was a post-processing issue with the ice shape of the experiment at − 5 °C and an icing duration of 60 s. Therefore, the ice shapes from run number 116 at − 5 °C and an icing duration of 120 s was studied instead.

Numerical Simulation

The ice accretion simulations conducted in this paper were done using ANSYS FENSAP-ICE [29] version 22.1 for the 2D simulations and version 22.2 for the 3D simulations. There are three modules utilized in an ice accretion simulation: FENSAP, DROP3D, and ICE3D. Each module calculates different steps of the icing process. It is possible to conduct multi-shot simulations with a new mesh generated between each step to incorporate the accumulated ice. The airflow and droplet

impingement is also recalculated using the new mesh, which then produces a new layer of ice accretion on top of the existing one. The steps are done iteratively for the whole simulation duration. The simulations in this paper were done in a 10-shot multi-shot simulation with a custom Fluent Remeshing script.

The airflow is set as steady state. The spatial discretization is done through a weak Galerkin finite element method [30]. Turbulence in the flow is modeled by applicating the Reynolds Averaged Navier-Stokes equations and a turbulence model. The simulations were performed using the Spalart-Allmaras turbulence model. Ozcer et al. [31] prefer utilizing the Spalart-Allmaras turbulence model, especially for multishot simulations as the model performs well when calculating turbulence and heat transfer on iced surfaces. The simulations are configured as fully turbulent. This decision is made, as the increased surface roughness due to ice would cause the transition from laminar to turbulent boundary layer to happen at the leading edge [12].

The droplet impingement in this paper is calculated in the DROP3D module of FENSAP-ICE, which can determine the mass of water captured by the geometry and the impingement limits [32]. The module implements an Eulerian two-fluid model consisting of the Euler or Navier-Stokes equations for inviscid and viscous flows respectively, extended by the particle continuity and momentum equations [30, 33]. In the Advisory Circular No 20-73A [9], the Federal Aviation Administration suggests the use of the Langmuir-D [34] droplet distribution for MVDs below 50 µm [33]. However, the simulations in this paper were conducted using a monodisperse distribution instead as the results using this distribution in the work of Fajt et al. [15] is shown to be sufficient.

The ICE3D module, which is a finite volume model, calculates the ice accretion rate by using the friction force and heat flux information from FENSAP and the mass rate of droplet impingement obtained from the DROP3D module [35]. The model is based on a set of partial differential equations of conservation [36], which was derived from the Messinger model [37] and further adapted to calculate ice accretion and water runback. The ICE3D module is also capable of calculating the required anti-icing loads to prevent ice on the walls of the geometry at a specific icing condition. Two available mass and thermal balance scenarios are running wet and fully evaporative. The running wet scenario calculates the heat flux necessary to maintain the water film at 0 °C so that no ice forms. On the other hand, the fully evaporative scenario determines the minimum required anti-icing loads to evaporate all impinging water droplets.

Validation Data

The experimental ice shapes from a study by Han, Palacios, and Smith [38] were chosen to validate the ice accretion simulations in this paper. The geometry used in the study is an untampered, non-swept, and no-twist blade with a 10.5-inch chord length and a NACA 0012 cross-sectional profile. The ice shapes were taken at 95% of the blade radial position by means of a 3D laser scanning method. The runs chosen for the validation data are cases number 14 and 29 to simulate rime and glaze ice conditions, respectively. The testing conditions are presented in Table 1. It is important to note, that the experiments performed were conducted at a higher Reynolds number regime than the planned rotor simulations. This leads to incorrect modeling of the boundary layer. However, due to limited available experimental data, the work of Han et al. [38] was still chosen to validate the simulation results.

Table 1: Selected testing conditions from the AERTS ice accretion experiments obtained from a study by Han et al. [38].

Case	Temp [°C]	V [m/s]	MVD [µm]	LWC [g/m^3]	Time [min]	AOA [°]
14	−15.4	56.2	28	0.44	4.1	3.5
29	−5.7	67.1	26.2	0.86	4.0	0

Geometries and Grid Setup

Three different geometries were used in this study. The verification and validation of the simulations were done on a NACA 0012 airfoil. The ice accretion simulations were performed on a 15-inch rotor to represent eVTOL UAVs and an 80-inch rotor to approximate a UAM eVTOL aircraft. The CAD models of the rotors were provided by the manufacturer [39]. The NACA 0012 airfoil was obtained from a database provided by Selig [40]. The rotor sections were created using the CAD software Siemens NX [41] and the mesh is generated using Pointwise [42] version 18.6. The ice accretion simulations in this paper start with a two-dimensional approach then followed by a simulation in 3D.

The 2D mesh is generated as an O-type grid with a far-field size of 20 times the airfoil chord length and an unstructured mesh. The airfoil geometry is split at approximately 20% from the leading edge to differentiate the parts mostly impacted by ice and to resolve them with more detail than the rest of the airfoil. The initial cell height of the grids is set between 1E−06 m and 5E−06 m depending on the airfoil size and a growth rate of 1.1 to achieve a dimensionless wall distance of y^+<1 for the first point. This step is necessary to ensure that the boundary layer and the viscous layer are well resolved, to correctly calculate the friction coefficients. Furthermore, the T-Rex function from Pointwise is applied to generate anisotropic layers at the boundary. The function is especially suitable for unstructured domains on geometries with high curvature [43]. The cell type is set to triangles and quads to enable anisotropic layers consisting of triangular and quadrilateral cells. Finally, the grid is extruded by 0.2 times the airfoil chord length in a spanwise direction. The reference area, which FENSAP-ICE requires to calculate the lift and drag forces, is obtained by multiplying the extrusion with the chord length.

NACA 0012

The NACA 0012 airfoil is chosen to mimic the geometry used in the validation data [38]. The geometry has a cross-sectional chord length of 0.267 m and it is neither swept, tapered nor twisted. The original NACA 0012 airfoil was obtained from a database by Selig [40]. For this study, the airfoil's trailing edge is modified using XFOIL [44] to get a blunt trailing edge with a 1 mm gap. This is done to achieve a more realistic geometry.

In addition to the initial mesh, a finer and coarser mesh is also generated for the NACA 0012 case. This is done to investigate the grid dependency. The additional meshes are created with a refinement ratio of $r = \sqrt{2}$. The initial cell height for all grids is set to 5E−06 m. The far-field size and the extrusion rate remain the same, while the growth rate is adapted. Figure 1 presents the NACA 0012 initial grid and a description of the grid setup is shown in Table 2.

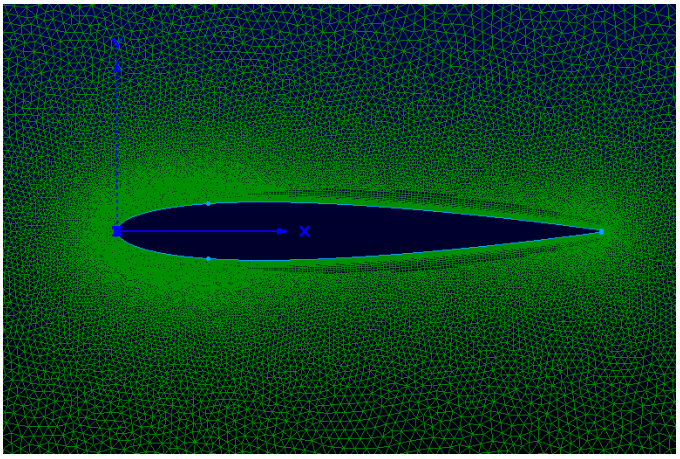

Figure 1: An illustration of the NACA 0012 initial mesh.

Table 2: Mesh features of the NACA 0012 ice accretion grid.

Mesh feature	Finer mesh	Initial mesh	Coarser mesh
Points on upper and lower side	255	180	130
Leading edge spacing [mm]	0.28	0.40	0.56
Trailing edge spacing [mm]	0.65	0.80	1.13
Points on far field inlet	850	600	425

Mejzlik 15-inch Rotor

The Mejzlik 15-inch rotor was chosen to represent the rotor size of an eVTOL UAV. The two-bladed rotor has a diameter of 15 inch and a 5-inch pitch at 75% blade radius. The CAD model of the rotor can be seen in Figure 2. It is a lightweight rotor designed for multicopter use. The rotor can spin up to 12000 RPM before the blade tips reach 0.7 Mach. It is the same rotor used in the ice accretion experiments.

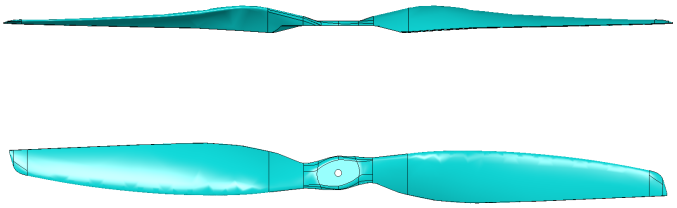

Figure 2: CAD model of the 15-inch Mejzlik rotor.

For the 2D ice accretion simulations, the cross sections of the blade were taken at three different radial positions. A description of the rotor sections including chord length and blade twist is presented in Table 3. To improve the mesh quality, the trailing edge of the sections has been modified to a blunt trailing edge in Pointwise. The grid generation generally follows the same workflow as with the NACA 0012. However, some differences had to be applied to account for the smaller, thinner airfoil cross sections. The differences to the initial mesh are presented in Table 4. The 3D mesh of the 15-inch rotor was created with a cylindrical far field with a distance of 10 times the blade radius to the rear and 5 times the blade radius to the front and sides. The blade leading edge is resolved with a constant 1024 points and the trailing edge has 1000 points. With a decay value of 0.5 and an initial cell height of 1E−06, the 3D mesh consisted of 6.5 million cells. A slice of the mesh is presented in Figure 3.

Table 3: Airfoil sections of the 15-inch rotor used for the 2D simulations.

Blade radius [%]	Chord length [cm]	Twist angle [°]
50	2.99	12.91
75	2.31	8.77
95	1.48	6.30

Table 4: Varying mesh features of the 15-inch rotor.

Mesh feature	50%	75%	95%
Leading edge spacing [mm]	0.05	0.04	0.02
Trailing edge spacing [mm]	0.10	0.08	0.04
Initial cell height [m]	2E−06	2E−06	1E−06

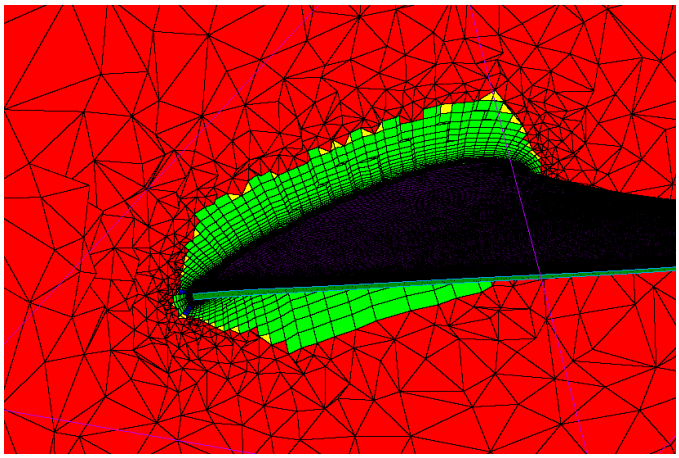

Figure 3: Slice of the 15-inch 3D mesh at 75% blade radial position.

Mejzlik 80-inch Rotor

The second rotor is an 80-inch rotor from the same manufacturer. This dimension is chosen to approximate the size of rotors utilized in UAM eVTOL aircraft. The rotor has a diameter of 80 inches and a 28-inch pitch at a 75% radius. An illustration of the rotor can be seen in Figure 4. The rotor is designed for high-performance multicopters and spins counterclockwise. The maximum rotation rate for the blade tips to remain subsonic is 2300 RPM.

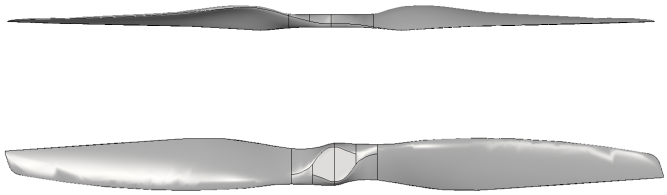

Figure 4: CAD model of the 80-inch Mejzlik rotor.

Similar to the 15-inch rotor, cross sections of the 80-inch rotor blade were taken in three positions: at 50%, 75%, and 95% radial position. The cross-sections were obtained using Siemens NX and exported to Pointwise for meshing. Table 5 presents a full description of the rotor sections. Due to its larger size, some meshing features were also adapted and thus differ from the verified mesh generation workflow. The upper and lower side of the airfoil was generated using 250 points, while the far field was defined with 800 points. The cell initial height for all 80-inch rotor sections is 2.5E−06 m. The leading edge and trailing edge spacing of the airfoil at 50% and 75% radial positions are 0.15 mm and 0.30 mm, respectively. The outer airfoil section at 95% of the blade radius has a finer leading edge spacing of 0.1 mm and a trailing edge spacing of 0.2 mm to better resolve the geometry. The 3D mesh of the 80-inch rotor was created with a sphere far-field with a sphere radius of 5 times the blade radius. The blade leading edge is set with a constant 1200 points and the trailing edge has 1000 points on both ends. With a decay value of 0.9 and an initial cell height of 1E−05 m, the 3D mesh consisted of 12.9 million cells. A slice of the mesh is presented in Figure 5.

Grid Dependence Study

Three separate grids with a constant refinement ratio of $r = \sqrt{2}$ were generated for the grid dependency study. The grid refinement ratio should not be less than 1.1 [45] to differentiate the discretization error from other computational errors. The features of all three grids are

Table 5: Airfoil sections of the 80-inch rotor used for the 2D simulations.

Blade radius [%]	Chord length [cm]	Twist angle [°]
50	16.03	12.97
75	12.36	8.82
95	7.91	6.00

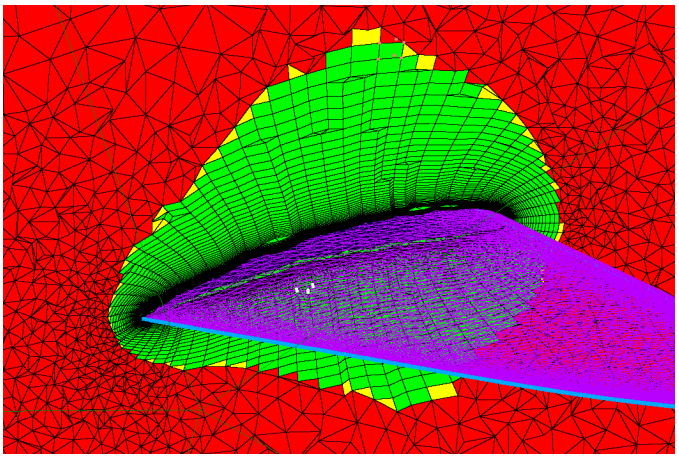

Figure 5: Slice of the 80-inch 3D mesh at 75% blade radial position.

presented in Table 2. The chord length of the airfoil is set to 0.266 m and the icing conditions follow the parameters used in the glaze and rime ice experiments by Han et al. [38]. A simulation is run for each grid resolution and both icing conditions. The lift and drag coefficients were chosen to investigate the grid convergence and plotted against the dimensionless grid spacing h. Should the results show a monotonous trend, the theoretical true value at zero grid spacing can be calculated using the Richardson extrapolation [46, 47].

Atmospheric Icing Conditions

The icing conditions used for the 15-inch rotor simulations are presented in Table 6. The values were chosen to replicate the icing conditions during the icing wind tunnel experiments. Table 7 describes the icing conditions for the 80-inch rotor simulations, which were derived from Appendix C. An MVD of 20 µm and a temperature of − 2 °C was chosen as it is the worst-case scenario for icing on the wing of a UAV [15]. A simulation at −5 °C is conducted to predict how the ice accretes in mixed ice conditions. Previous studies on a UAV propeller [48] show that lower temperatures tend to have larger performance degradation. Therefore, the rotor is also simulated at a temperature of −15 °C. The icing duration was decided based on a UAM aircraft mission profile estimation. To simplify the simulation, the transition and climb phase is omitted in this paper and the UAM eVTOL is assumed to climb vertically from ground level to its cruising altitude. An icing time of 300 seconds was decided to illustrate a fully vertical take-off to a cruising altitude of 1500 ft with a climb rate of 1.5 m/s.

Table 6: Icing conditions for the 15-inch rotor simulations based on the VTT IWT experimental test runs.

Case	Temp. [°C]	MVD [μm]	LWC [g/m^3]	Time [s]
Glaze	−5	24.3	0.41	120
Mixed	−10	24.3	0.41	60
Rime	−15	24.3	0.41	60

Table 7: Icing conditions for the 80-inch rotor simulations derived from the Appendix C.

Case	Temp. [°C]	MVD [μm]	LWC [g/m^3]	Time [s]
Glaze	−2	20	0.59	300
Mixed	−5	20	0.53	300
Rime	−15	20	0.32	300

Flow Conditions

The rotors studied in this paper rotate with a rotation speed of 5000 RPM for the 15-inch and 1500 RPM for the 80-inch, which translates to a tangential velocity at the blade tip of approximately 100 m/s and 160 m/s for the small and large rotors, respectively. The rotation speed of the small rotor was chosen to match the setup used in the VTT IWT icing experiments, while the rotation speed of the large rotor was chosen so the rotor can generate approximately 900 N of thrust and the blade tips remain below Mach 0.7. An additional vertical wind speed of 6 m/s, which is classified as a moderate wind in the Beaufort scale [49], is additionally implemented. The rotor flapping, coning, and ground effects are not taken into consideration in this paper. The rotational relative inflow is obtained by adding the local tangential velocity due to rotation and the wind speed. The induced flow is the downward displacement of air caused by the horizontal motion of a moving object [50]. A summary of the velocity components used in this paper is presented in Table 8.

Considering the variable angle of attack depending on blade location and airspeed [50], the air velocity in the 2D simulations within this paper was set to its local resultant relative wind without a velocity angle since the angle of attack is within the blade twist angle. The local angle of attack can be approximated by subtracting the angle between the resultant relative wind and the rotor disk from the blade twist angle and is presented in Table 9. The local blade twist angles can be found in Table 3 for the 15-inch rotor and in Table 5 for the 80-inch rotor. There are several published works available presenting studies and suggestions on the angle of attack determination of rotor blades, for example, the study by Shen et al. [51]. However, the exact calculation of the angle of attack is not within the scope of this paper. Therefore, an approximation was done instead.

Table 8: Velocity components of the flow applied to the 2D simulations within this paper.

Rotor	**15 inch**			**80 inch**		
Blade radius [%]	50	75	95	50	75	95
Local tangential velocity [m/s]	49.87	74.81	94.76	79.79	119.69	151.07
Rotational relative wind [m/s]	55.87	80.81	100.75	85.79	125.69	157.61
Induced flow velocity [m/s]	13.77	9.18	7.24	21.34	14.23	11.23
Resultant relative wind [m/s]	57.54	81.32	101.01	88.41	126.49	158.01

Table 9: Local angle of attack and the angle between the relative wind and the rotor disk for all studied airfoil sections.

Rotor	**15-inch**			**80-inch**		
Blade radius [%]	50	75	95	50	75	95
Angle of incidence [°]	13.84	6.48	4.11	13.97	6.45	4.07
Angle of attack [°]	−0.93	2.28	2.18	−1.00	2.36	1.92

Results

Grid Dependence Study

The results of the grid dependency study are plotted against the dimensionless grid spacing *h* in Figure 6 for the rime ice case and in Figure 7 for the glaze ice case. Only the drag coefficients of the glaze ice case present a monotonic trend. Therefore, a Richardson extrapolation can only be performed on the coefficients of the glaze ice case. The order of grid convergence was calculated and then applied to the Richardson extrapolation equation. As shown in Figure 7b, the hypothetical exact solution is shown to converge. Furthermore, the grid convergence index (GCI) values and the asymptotic range of convergence were calculated. The CGI values for the coarser and finer grids are 9.41% and 2.97%, respectively, and the asymptotic range of convergence comprises a value of 1.0502. The results indicate that the error band is narrow as the CGI values signify the error between the grids [52] while an asymptotic range of approximately one implies that the grids are sufficiently refined [45], which is what the glaze ice drag coefficient calculation results in this grid dependency study suggest.

The calculated lift coefficient of the glaze ice case, as illustrated in Figure 6a, shows discontinuity with the initial mesh calculating a lift coefficient of −0.7164E−04 while the fine and coarse mesh result in a positive lift coefficient of −1.201E−04 and −1.124E−04 respectively. However, it is important to note that the studied NACA 0012 airfoil is symmetrical. In the glaze ice case, the simulation is run at 0° angle of attack, which in theory produces no lift [53]. With the simulated values being ten to the minus four power, the lift coefficient of the NACA 0012 in the glaze icing condition is virtually zero, thus in line with the theory. If we look at the lift coefficients of the rime ice case, it can be seen that the solutions lie within 0.18% – 0.22% from each other, while the drag coefficients are situated between 0.39% – 0.64%. Since the deviations between the results are minor, it is assumed that the effects of grid dependency are minimum and can be neglected for all meshes. The initial mesh setup is decided to generate the grids of the rotor sections.

Numerical Parameter Study

After investigating the grid convergence, the effects of various parameters are studied. The parameter study was done with the NACA 0012 initial mesh. First, the effect of the multishot simulation is studied. A multishot simulation consisting of 10 steps was performed on the NACA 0012. The results are plotted against a single shot simulation as presented in Figure 8. The rime ice case presents small differences. The multishot simulation is shown to have a more streamlined shape, while the total ice mass remains similar. A greater variety of ice shapes is observed in the glaze ice case with the multishot simulation delivering more details compared to the mainly rounded shape of the single shot simulation.

Second, the effect of the chosen CFD simulation software is examined. The simulations in this section were run using LEWICE and FENSAP-ICE. The results can be seen in Figure 9 that both codes can predict consistent rime ice shapes. However, a stark deviation is observed in the glaze ice shapes. The LEWICE code underpredicts the total ice mass and delivers fewer horn ice features compared to FENSAP-ICE. This is agreeing with the observation by Hann [54] for simulations with the NREL S826 airfoil. The level of aerodynamic penalties due to icing and the heat flux required to mitigate it depends highly on the formed ice shapes as it dictates how the flow physics change [12]. Therefore, capturing the ice features is regarded as important and the use of FENSAP-ICE for the icing simulations is decided.

Ice Accretion Simulation Validation

Following the grid dependency and the parameter study, the simulation results are compared to the experimental ice shapes obtained by Han et al. [38] to validate the 2D simulations. The numerical ice shapes were calculated using the parameter setup listed in Table 10. A specified sand grain roughness with a Nikuradse equivalent roughness height of 0.5 mm was selected, which is the default setup in FENSAP-ICE [33]. The icing conditions were set to match the conditions used in the experiments and it is presented in Table 1 for both rime and glaze ice cases. The simulations were conducted using the Spalart-Allmaras turbulence model and the flow is set to fully turbulent.

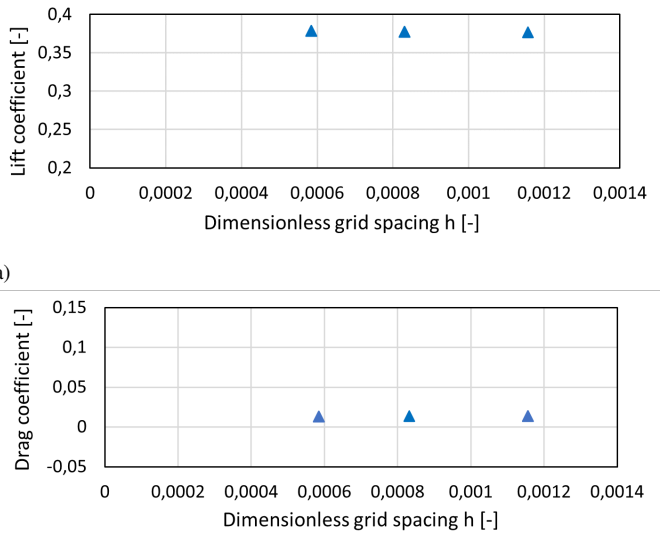

Figure 6: Lift (a) and drag (b) coefficients of the rime ice simulations for the grid dependency study.

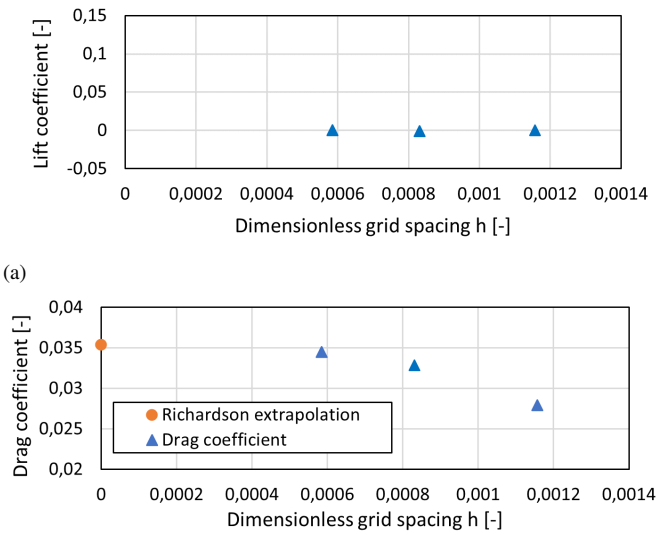

Figure 7: Lift (a) and drag (b) coefficients of the glaze ice simulations for the grid dependency study.

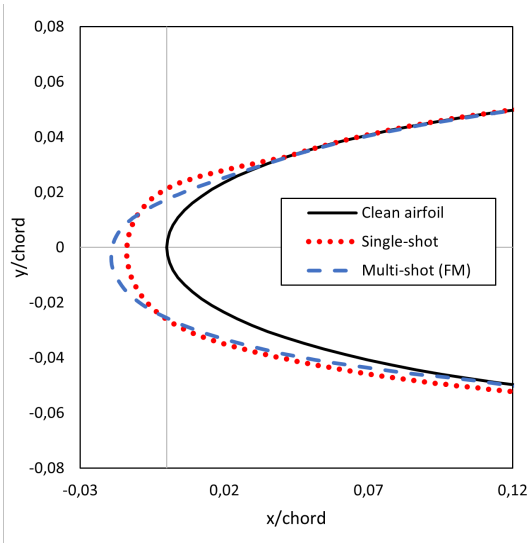

(a)

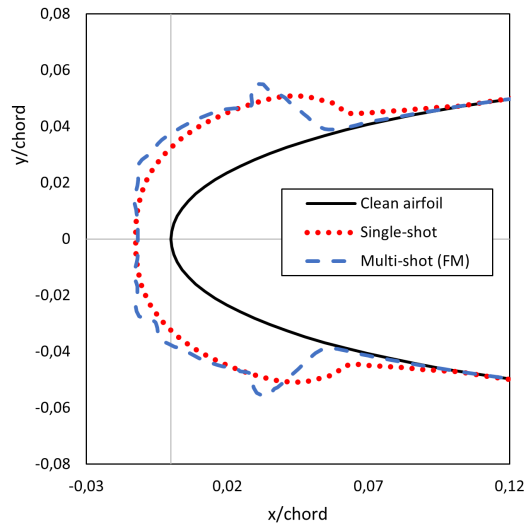

(b)

Figure 8: A comparison of the results from a single shot and multi-shot simulation for the rime (a) and glaze (b) ice case.

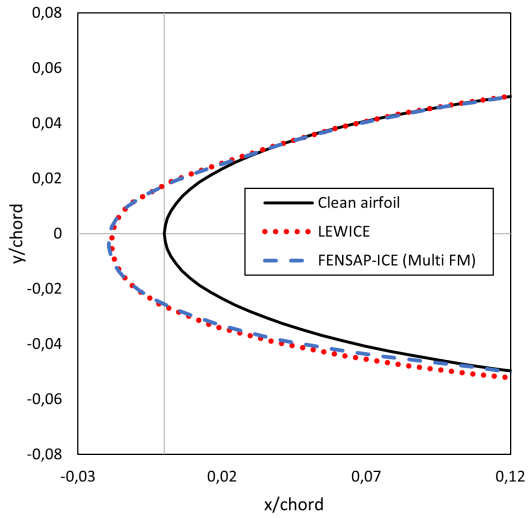

(a)

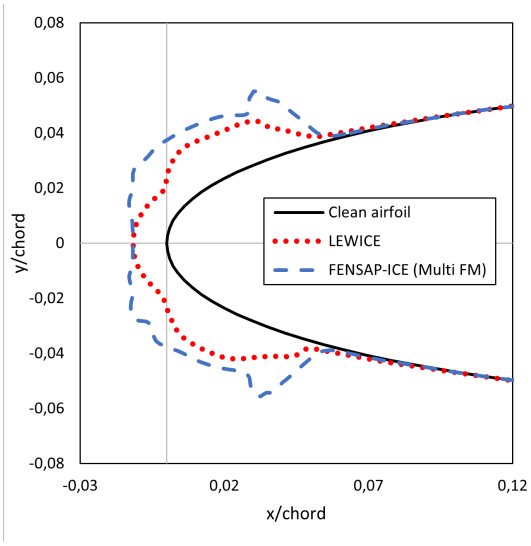

(b)

Figure 9: A comparison of the simulation results using LEWICE and FENSAP-ICE codes for the rime (a) and glaze (b) ice case.

Table 10: Parameter setup for the ice accretion simulation.

FENSAP	
Turbulence model	Spalart-Allmaras
Boundary layer	Fully turbulent
Surface roughness	Specified sand grain 0.0005 m
Artificial viscosity	Streamline upwind + cross wind dissipation 1E–07
DROP3D	
Physical model	Droplets
Distribution	Monodisperse
Water density	1000 kg/m^2
ICE3D	
Ice - Water model	Glaze Advanced
Roughness output	Sand grain from beading
Time step	Automatic
Grid displacement	10 shot multishot, custom Fluent Meshing

The simulation results compared to the experimental data set are presented in Figure 10. For the rime ice case, the simulation correctly captures the upper and lower icing limits and the streamlined shape while slightly overestimating the total ice thickness. This difference could be caused by the applied turbulence model which could only approximate the turbulence occurring and not resolve it. Nevertheless, the simulation can reproduce the general rime ice shape of the experiment with minor discrepancies. Therefore, one may conclude that the simulation model is suitable for rime icing conditions. In the glaze ice case, the ice thickness at the leading edge is shown to be underpredicted by the simulation. The ice shapes at the upper and lower side of the airfoil at approximately 4% of the chord are also significantly thinner when compared to the experimental results. The pressure side of the airfoil presents more feathering ice shapes in the experiment, which is lacking in the numerical result. This could be caused by the ice horns formed in the numerical ice shapes. The flow field behind an ice horn is characterized by large separation regions [12], thus hindering the ice growth behind the region. Glaze ice shapes are typically more complicated to predict properly due to the heat transfer mechanics, whereas the droplets in rime ice cases freeze immediately upon collision [55].

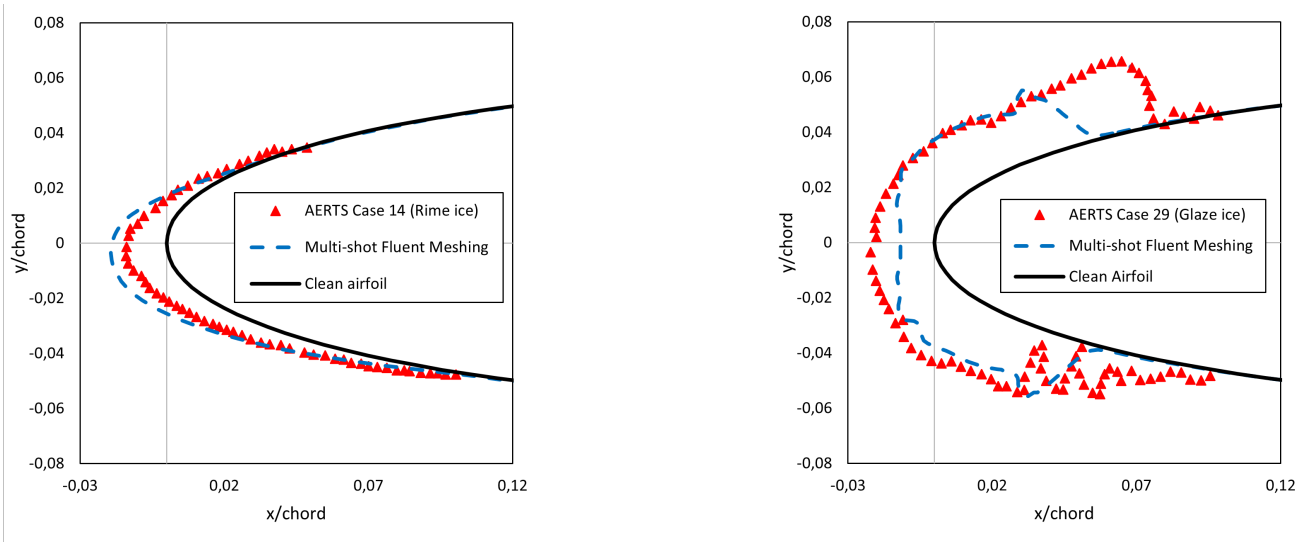

(a) (b)

Figure 10: Results of the NACA 0012 ice accretion simulation in rime (a) and glaze (b) icing conditions in comparison with the AERTS experimental results [38].

Ice Accretion Experiment and Simulation Results

In the scope of this paper, ice accretion experiments and simulations were conducted. The ice accretion experiments were conducted on the small 15-inch rotor in an icing wind tunnel, while the ice accretion simulations were calculated for both rotors. The results of the ice accretion experiments are presented in Figure 11 alongside the simulation results of the 15-inch rotor. The experiment results show significant buildup around the airfoil's leading edge in general. The most ice accumulation relative to the airfoil size is shown at the tip of the blade in the airfoil at 90% radial position with typical rime ice shapes appearing in lower temperatures such as – 10 °C and – 15 °C. For the inner sections of the blade, at 50% and 75% of the blade radius, the most ice mass accumulated is shown at a temperature of – 5 °C. This is the result of the longer icing duration of the glaze ice case. The ice shapes at – 5 °C present an irregular, with small ice horns forming especially at the upper part of the leading edge. At lower temperatures in the airfoil, the ice forms multiple ridges at the further parts of the airfoil until ca. 15% of the chord length.

For the 2D ice accretion simulations of the 15-inch rotor, it can be seen for the 15-inch rotor that all sections show significant ice accumulation in the leading edge of the airfoil. There are no visible ice shapes formed on the suction side of the airfoil, although surface roughness due to ice may occur. Ice horn shapes can be observed in all glaze icing conditions with the most prominent being towards the tip of the blade at 95% radial position. It is observed that the predicted ice shapes for icing temperatures of −10 and −15 °C are similar. In the two colder icing conditions, the simulation predicts a typical rime ice shape for the airfoils closer to the rotor center. At the tip of the blade, the ice accretion formed a small horn on the upper side of the ice. At 95% of the blade radius, the airfoil is considerably smaller and thinner compared to the inner parts of the blade. This leads to a higher droplet collection efficiency. The blade tip also experiences the largest local tangential speed due to rotation, which generally increases the stagnation temperature. However, in the 15-inch case with a simulated rotor rotation of 5000 RPM and an air temperature of −15 °C, the adiabatic stagnation temperature at 95% of the blade radius is −9.92 °C and therefore allowing the water droplets to freeze. It should be mentioned that the icing duration of the 95% airfoil in – 5 °C was reduced from 120 s to 60 s due to remeshing failures at the 8th multishot step.

The 3D icing simulation of the 15-inch rotor was calculated at −10 °C and with a rotation rate of 5000 RPM for 60 seconds. At −10 °C the ice accretion presents a shape typical of rime ice for all rotor sections. The form appears more rounded compared to the 2D simulation results, which tend to grow longer. The ice in the 3D simulation accumulates more on the upper side of the airfoil leading edge, again contrasting the trend of the 2D simulations. Less ice build-up is observed surrounding the trailing edge in the 3D simulations with the most accretion occurring at 95% blade radius. The ice accretion at −10 °C for the 15-inch rotor is seen covering the whole blade length in Figure 12.

The ice accretion simulation results for the large 80-inch rotor sections are presented in Figure 13. In general, the ice shapes obtained differ from the 15-inch rotor sections. The ice accretion at the blade tip in rime icing conditions shows the most similarities between the rotors, as both simulations predict a significant ice accumulation at the leading edge. There is no ice accretion at the 95% airfoil for the temperatures closer to the freezing point. This is owed to the adiabatic stagnation temperature, which is influenced by the local Mach number, increasing the local temperature above the freezing point [17]. At – 2 °C icing condition, the lack of ice due to the heightened stagnation temperature was similarly observed at the 75% airfoil. The ice accumulated on the pressure side of the airfoil with a constant thick layer at 75% radius and an irregular shape forming at 50% of the blade. In the rime ice case, the inner airfoils form rather uniform ice shapes without ice horns. For the – 2 °C icing condition, the simulation predicts notably less ice accretion compared to other temperatures. However, at 50% blade radius small ice horns were simulated around the upper part of the leading edge, which lead to large flow disturbance aft of the ice as displayed in Figure 14.

The large 80-inch rotor 3D simulation was run at −15 °C with 1500 RPM for 300 seconds. The ice-shape cross-sections of the 80-inch rotor are presented in Figure 15. The most significant difference between the 2D and 3D ice accretion simulations is the absence of ice in the 3D results in the outer area of the blade from approximately 80% of the blade radius, as seen in Figure 16. Consequently, there is no ice at 95% blade despite the 2D simulation predicting ice accretion. The airflow solution of the 80-inch rotor simulation in 3D shows positive total temperatures starting from approximately 78% of the blade radius towards the blade tip. This coincides with the freezing fraction of the 80-inch rotor and with the calculated ice accretion. The spikes forming at the tip of the large rotor may be an error caused by the boundary setting of the mesh

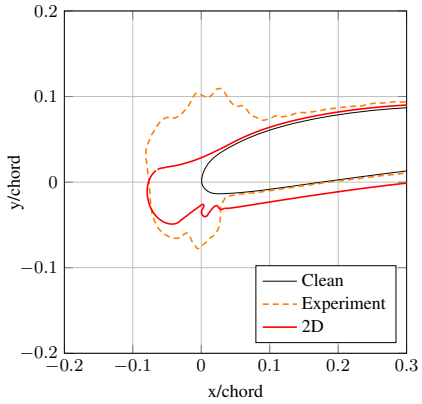

(a) Ice shapes at −5 °C at 50% of the blade radius.

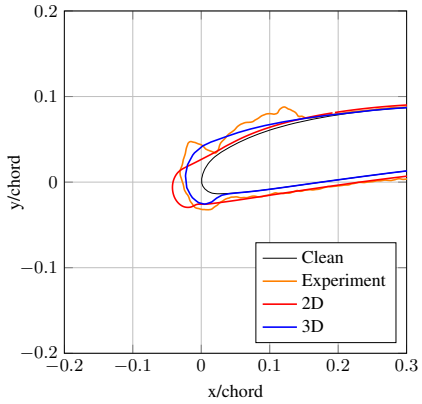

(b) Ice shapes at −10 °C at 50% of the blade radius.

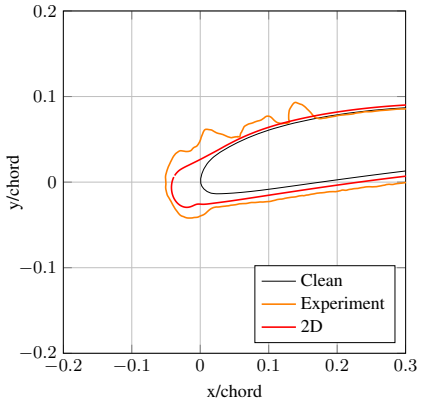

(c) Ice shapes at −15 °C at 50% of the blade radius.

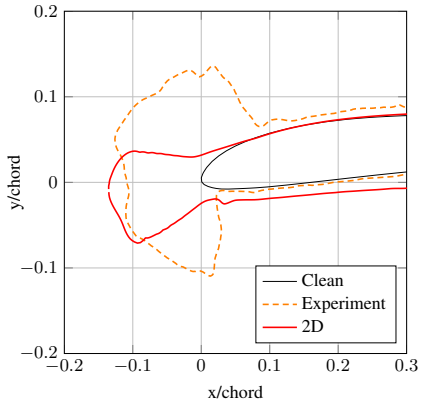

(d) Ice shapes at −5 °C at 75% of the blade radius.

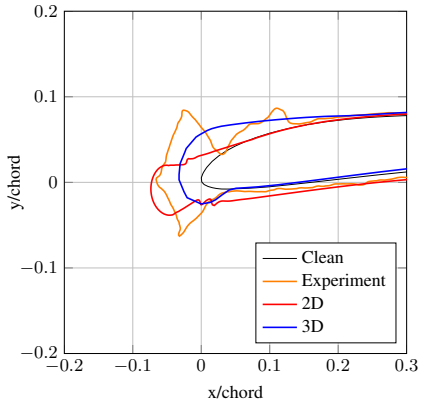

(e) Ice shapes at −10 °C at 75% of the blade radius.

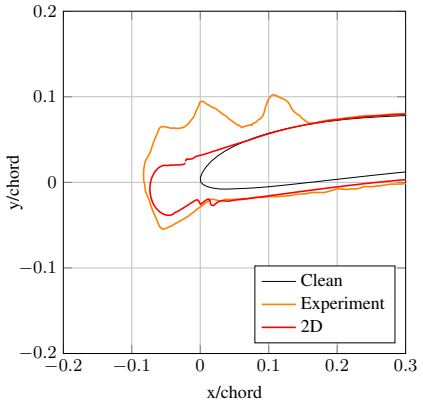

(f) Ice shapes at −15 °C at 75% of the blade radius.

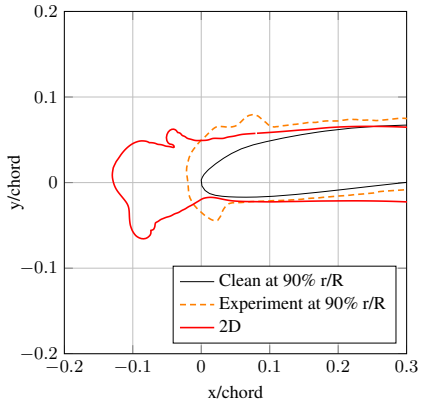

(g) Ice shapes at −5 °C at 95% of the blade radius for the numerical ice shapes and at 90% radial position for the experimental ice shape.

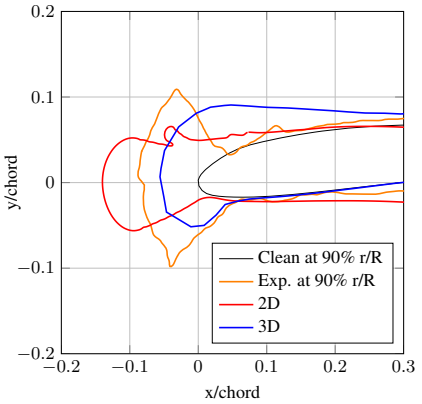

(h) Ice shapes at −10 °C at 95% of the blade radius for the numerical ice shapes and at 90% radial position for the experimental ice shape.

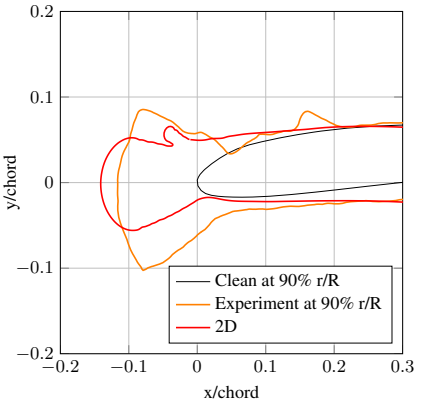

(i) Ice shapes at −15 °C at 95% of the blade radius for the numerical ice shapes and at 90% radial position for the experimental ice shape.

Figure 11: Results of the ice accretion experiments and simulations of the small 15-inch rotor at various temperatures with a wind velocity of 6 m/s and a rotation rate of 5000 RPM.

Figure 12: Ice shape of the 15-inch rotor at −10 °C obtained from a 3D ice accretion simulation.

since an ice accretion of this kind has not been observed in real life to the author's knowledge. The ice forming in the inner side of the 80-inch rotor blade appears to have typical rime ice shapes. There is no ice accretion predicted at the trailing edge of the 75% section, contrasting the 2D solution. The ice on the leading edge appears more streamlined in the 2D results compared to the 3D. At a 50% blade radius, the ice accumulates more on the upper side of the airfoil leading edge compared to the solutions in 2D.

Performance Degradation Simulation

Following the ice accretion simulations, the aerodynamic penalties due to icing were investigated. This study is done for the −15 °C temperature for both rotors and at the temperature nearest to the freezing point, which would be − 5 °C for the 15-inch and − 2 °C for the 80-inch rotor. The ice shape and roughness distribution obtained from the 2D ice accretion simulation were used. In the FENSAP configuration window under the surface roughness option, the roughness output file from the 2D ice accretion simulation can be uploaded for the performance degradation simulation. The airflow is calculated for the angle of attacks between − 10° to 10° and considering the local blade twist angle. The performance of the ice-free airfoil is similarly calculated, and the results are compared with the iced airfoil polars. The performance simulations predict an increased drag and reduced lift in the entire range of angle of attack and for all calculated airfoil sections. This is most likely caused by the increased roughness and surface area due to ice accretion and flow separation aft of the ice shape.

Figure 17 presents the performance degradation of the small 15-inch rotor section at 75% blade radius. For the rime ice case, a stall angle reduction of approximately 2.5° is observed, as well as a slight performance deterioration along the linear part of the polar. The drag coefficients of the rime ice case experienced the same penalties as the iced airfoil displaying a visible increase compared to the clean airfoil. The glaze ice case displays a more prominent degradation. However, it should be noted that the glaze ice shape is significantly larger than the rime ice shape as it was simulated with double the icing duration. The stall angle is reduced by roughly 5°, as illustrated in Figure 17c. The lift performance along the linear part is reduced even further compared to the rime ice case. Similar behavior is observed for the drag coefficients.

Figure 19 displays the aerodynamic penalties of the 80-inch rotor at 75% blade radius for the rime ice case and at 50% for the glaze icing condition. The different rotor sections had to be chosen for the glaze ice case because there was no ice accretion for this icing condition at 75% blade radius. The drag increase for the 80-inch rime ice case appears to be smaller in comparison to the 15-inch rime, although it is still not negligible as illustrated in Figure 18b. The lift reduction caused by rime ice is observed to be greater than for the 15-inch rotor section. However, the stall angle reduction is less eminent with a 1° change. The same could not be said for the glaze ice case. Figure 19a shows a significant reduction in the lift and the stall angle of the glaze ice case at 50% of the blade. The drag coefficients of the 80-inch 50% airfoil show a noteworthy increase compared to the rime ice case. This could be due to the flow separation following the ice horn at the upper side of the leading edge, as presented in Figure 14.

Anti-icing Loads Simulation

To design and develop a thermal ice protection system (IPS), information regarding the required heat flux is required. The anti-icing load simulations in this paper were conducted at −15 °C. There are two heat flux distributions available in FENSAP-ICE: fully evaporate and running wet. The fully evaporative scenario requires enough heat flux to evaporate all impinging water droplets, while the running wet condition sets the surface temperature to 0 °C so water can flow back. This leads to a higher maximum heat flux required for the fully evaporative scenario, as observed in Figure 20 for the 15-inch rotor sections and in Figure 21 for the 80-inch, where the scenario requires at least double the amount of heat compared to the running wet condition for all blade sections in both rotors. The area where the maximum amount of heat flux is required is located slightly below the tip of the airfoil leading edge. This is where most ice accumulated for this specific icing condition and considering the local blade twist angle. The required heat flux of every rotor section for both conditions is presented in Table 11. It is shown that the full evaporative scenario requires around 13% to 43% more heat compared to the running wet condition. For both the 15-inch and 80-inch rotors, the blade tip area requires less heating than the inner sections. This may be attributed to the smaller surface area of the blade's outer section compared to its mid and inner sections.

Table 11: Fully evaporative and running wet heat flux requirements for the blade sections of both rotors at an air temperature of −15 °C.

Rotor	Radial position	FE Requirement (W)	RW Requirement (W)	Difference in %
15-inch	50%	5.83	3.47	40
15-inch	75%	4.11	3.02	26
15-inch	95%	1.90	1.65	13
80-inch	50%	122	84.7	30
80-inch	75%	99	60.5	39
80-inch	95%	44.6	25.4	43

Discussion

Ice Accretion Experiments and Simulation

As presented in the previous section, the results show that the obtained ice shapes depend strongly on the icing condition. This agrees with the observation by Fajt et al. [15] on UAV wings. The icing condition dependency of the numerical ice shape is seen, for example, by the similar results obtained from the 15-inch 2D simulation at −10 °C and −15 °C where only the air temperature was different while the icing duration, LWC, and MVD setting are the same. This may be due to the freezing fraction of the − 10 °C case, which is already approximately 1, thus bringing no further changes when lowering the temperature even further. Results in this paper are also consistent with the works of Hann and Johansen [11] regarding the influence of airfoil chord length on ice accretion. In the 2D simulations for both rotors in rime icing conditions, the outer blade section at 95% radial position presents the most ice accretion relative to the airfoil size. In low icing temperatures, the water droplets tend to freeze rapidly upon impingement. The airfoil chord length and leading edge diameter at the blade's tip are significantly smaller than the inner airfoil sections,

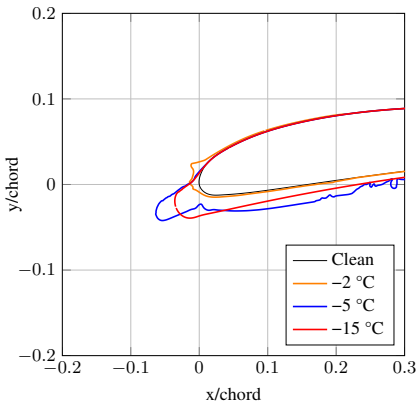

(a) 50% of the blade radius.

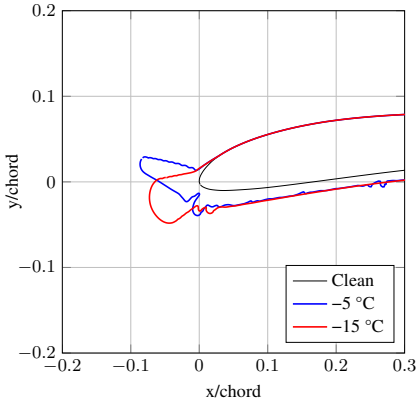

(b) 75% of the blade radius. No ice accretion for the simulation at −2 °C.

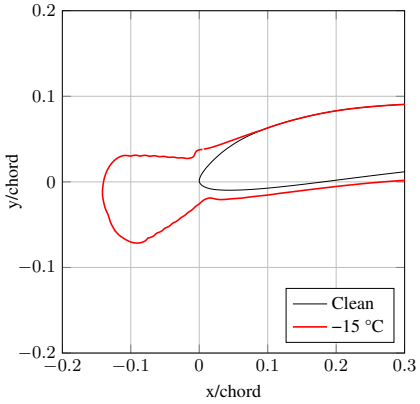

(c) 95% of the blade radius. No ice accretion for the simulation at −2 °C and −5 °C.

Figure 13: Results of the 2D ice accretion simulation on the 80-inch rotor blade sections.

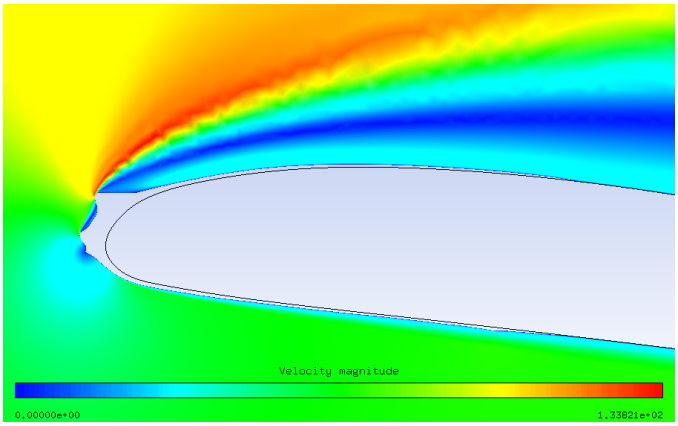

Figure 14: Large flow separation following the accreting ice at the leading edge of the 80-inch rotor section at 50% of the blade, glaze icing condition at −2 °C.

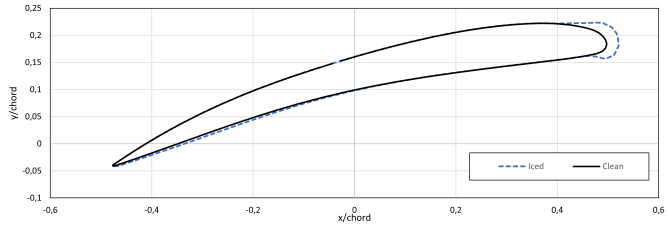

(a) 50% of the blade radius.

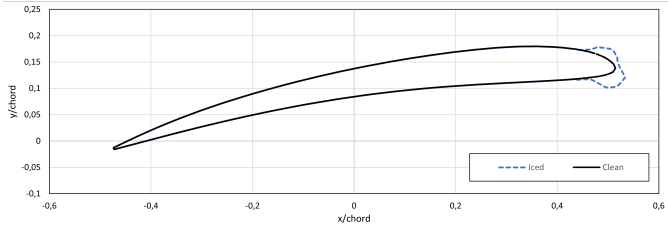

(b) 75% of the blade radius.

Figure 15: Ice shape cross-sections of the 80-inch rotor obtained from the 3D ice accretion simulation at −15 °C, 1500 RPM, an icing duration of 300 s an LWC of 0.32 g/m^3, and an MVD of 20 µm.

which gives them less impact on the surrounding far field and consequently leads to a higher collision rate. This and the local airspeed acting on the airfoil lead to a higher ice accretion rate at the

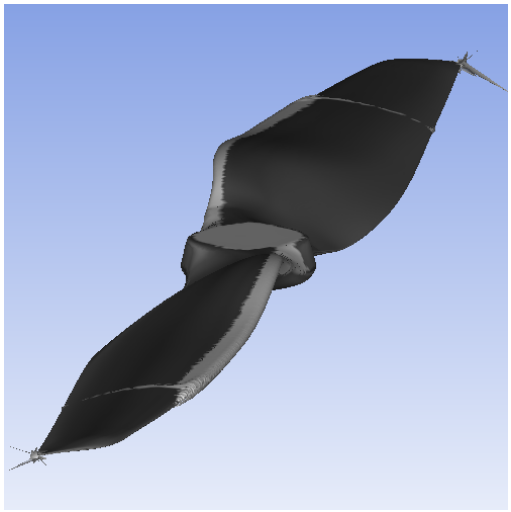

Figure 16: Ice shape of the 80-inch rotor at −15 °C obtained from a 3D ice accretion simulation.

tip area of the blade. This supports the observations by Müller et al. [23], which suggests that the rotational speed of a rotor plays a role in the final ice accretion shape and thus should be treated as an independent parameter. This would again emphasize the sensitivity of rotating lifting surfaces on icing compared to a fixed surface. The ice accretion study on the PX-31 Falk by Fajt et al. [15] was conducted for an icing duration of 20 minutes and for a significantly larger airfoil, whereas the rotor simulations in this paper were done at a considerably lower duration, ranging from 1 to 5 minutes of icing time. This would indicate a greater need for icing studies on rotating lifting surfaces, such as rotors and propellers.

Compared to the experimental ice shapes, the predicted numerical ice shapes of the 15-inch rotor show a more rounded shape even for the glaze icing condition, which is typically irregular. The ice experiments show similar ice accretion near the blade tip at −5 °C with the simulation results. At −10 °C and −15 °C the experiments display an approximately similar amount of ice mass accretion to the numerical solution, albeit with a varied general shape. The experimental ice shapes in − 15 °C display sharp ice horns despite being tested at a typically rime icing condition. This contrasts the rounded ice shape from the simulations, save from the ice accretion at 95% which approximated the ice accumulation at the leading edge. Müller et al. [23] investigated the numerical ice accretion on a UAV propeller. At 21 inches, the studied propeller has a slightly larger diameter

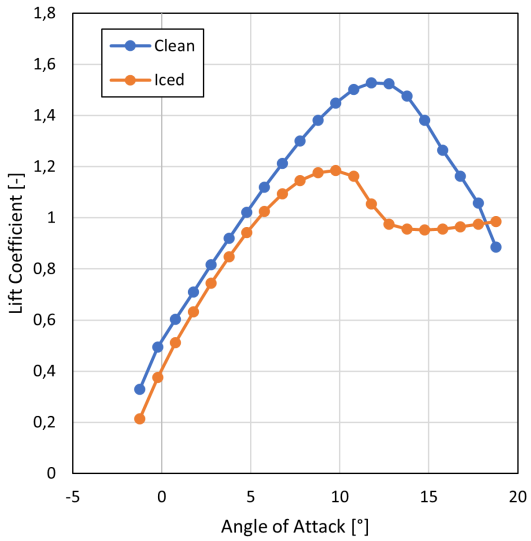

(a)

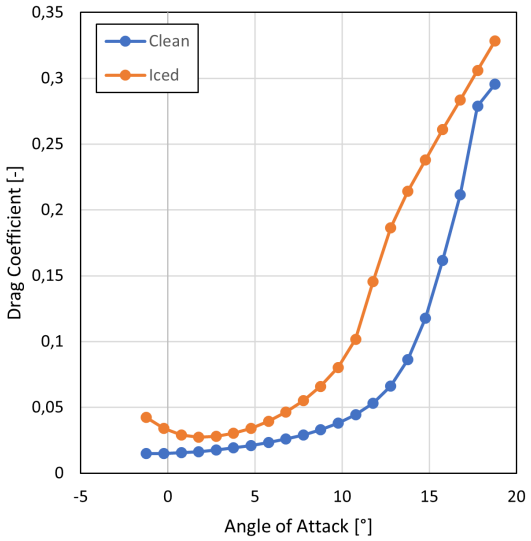

(b)

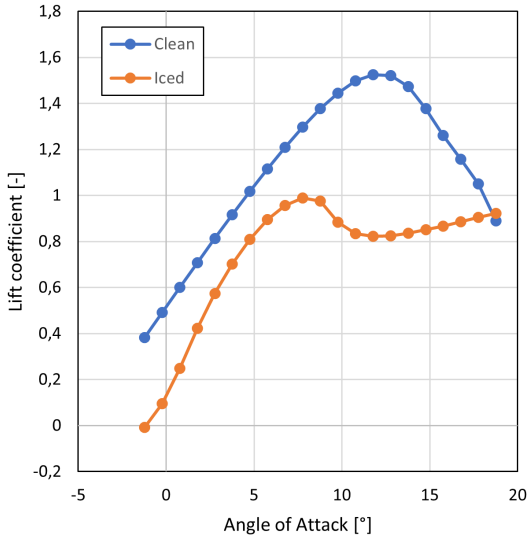

(c)

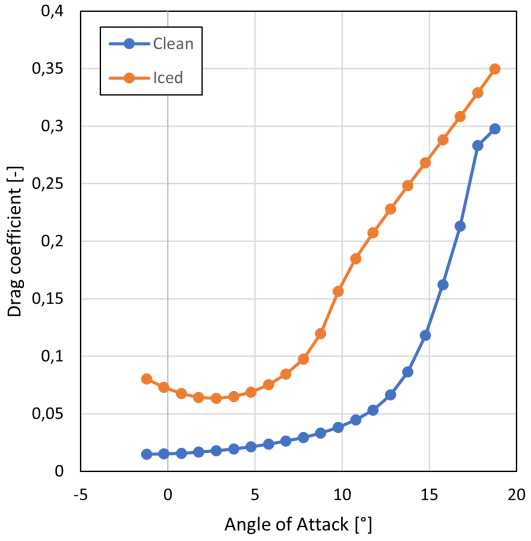

(d)

Figure 17: Degradation of the lift coefficient (a) and the drag coefficient (b) due to ice accretion at −15 °C of the 15-inch rotor at 75% blade radial distance.

compared to the 15 inches used in this paper and in the experiments. Comparing the numerical ice shapes obtained in this study with the experimental ice shapes, it can be seen that the propeller simulations display more ice horn shapes specifically at −5 °C. At −15 °C, both numerical ice shapes predict a significant amount of ice accretion and in a shape that commonly represents rime ice.

Compared to the numerical ice shapes of a UAV propeller studied by Müller et al. [23], the eVTOL small rotor ice shapes show less horn ice formation and more bulky accretion around the leading edge for the −5 °C icing temperature. Large ice accretion means an increase in surface area, which in turn increase the airfoil drag and the droplet accumulation rate. For the ice accretion simulation at −15 °C, both numerical results display a similar typical rime ice shape. This would imply that the direction of airflow with regards to the rotating axis influences the ice shapes in glaze icing conditions particularly. This adds another point to the notion of glaze ice simulation being more challenging to conduct compared to rime, as it has been observed in previous studies [55]. The ice shape cross-section of the 2D simulations in low temperatures generally shows a close approximation with the experimental ice shapes, with the exception of the sharper details and forming ice feathers. This could imply that a 2D simulation is sufficient to predict the approximate ice shape of a rotor in icing conditions in which rime ice shapes are expected. The 15-inch 3D ice accretion simulation for −10 °C show that the ice formed for the whole blade length. This agrees with the experimental ice shape. However, the 3D simulation predicts a more streamlined ice shape compared to the experiments. This could be caused by the mesh resolution, which may not be sufficiently fine and was not further investigated for grid dependency.

The ice shapes formed on the 80-inch rotor blade sections in temperatures close to the freezing point show great deviation within a variety of icing temperatures and airfoil sizes. At −5 °C, the ice accretion is predicted to have the most mass and grow into highly irregular shapes with horns, which would lead to flow disruption aft of the ice and cause separation. The horn ice forming at −2 °C is shown to cause flow separation as illustrated in Figure 14 and lead to significant aerodynamic penalties as presented in Figure 19. However, the middle and outer airfoil sections show no ice accretion for −2 °C. As the ice shape dictates how the aerodynamic forces act on the iced rotor blade, further studies on how the ice horns grow in a spanwise

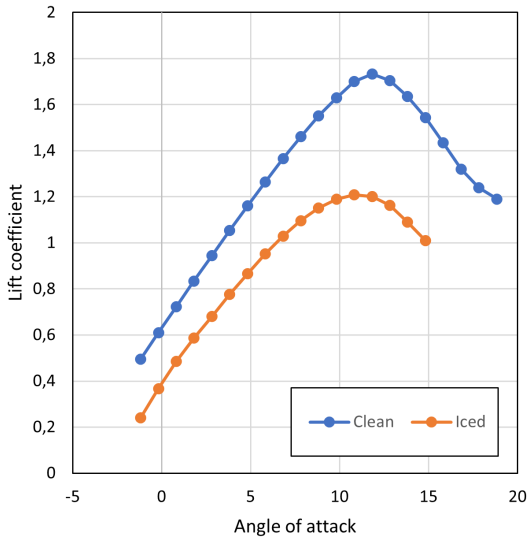

(a)

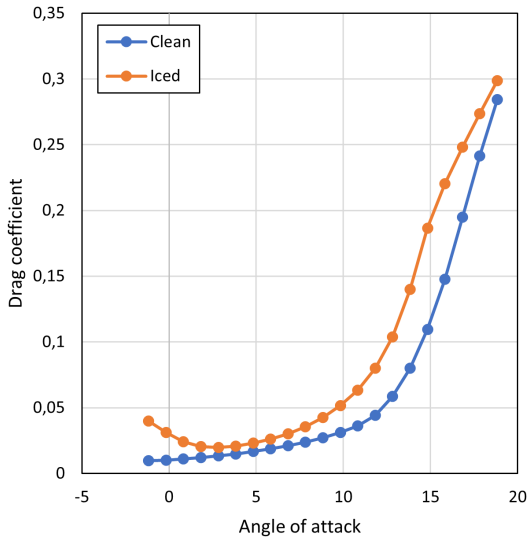

(b)

Figure 18: Degradation of the lift coefficient (a) and the drag coefficient (b) of the 80-inch rotor sections due to ice accretion in −15 °C at 75% blade radius.

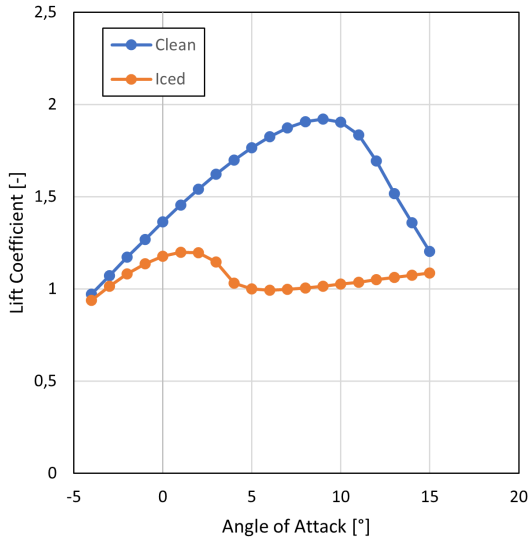

(a)

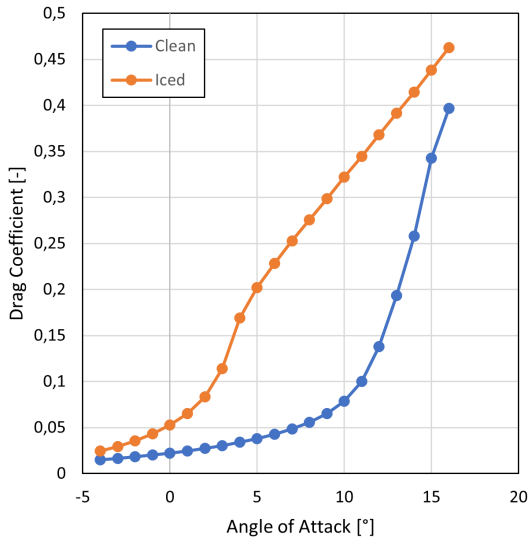

(b)

Figure 19: Degradation of the lift coefficient (a) and the drag coefficient (b) of the 80-inch rotor sections due to ice accretion in −2 °C at 50% blade radial distance.

direction would be of interest. The 3D ice accretion simulation of the 80-inch rotor in rime ice conditions predicted no ice accretion on the outer parts of the blade. This behavior also prevails in rotors and propellers of larger manned aviation vehicles due to higher stagnation temperatures which lead to substantial local temperature increase [17]. This deviation between the 2D and 3D results could also be caused by increased friction and three-dimensional crossflow, which increases the temperature in the 3D simulation compared to the 2D simulation. The airflow simulation of the large rotor shows positive total temperatures at the outer region of the blade. This would imply that the UAM eVTOL rotor behaves more like rotors in larger manned aviation than that of a UAV. The local Reynolds number of the 80-inch cross-sections ranges between Re = 0.95 – 1.18 10^6 depending on chord length, local airspeed velocity, and air temperature. This falls in between the upper range of a typical UAV operational Reynolds number, which is Re = 10^4 – 10^7, and the lower threshold of a larger manned aircraft at Re = 10^7 – 10^9 [19]. As a difference in the Reynolds number directly translates to the different physical behavior of the flow [20], thus influencing the ice accretion process, this must be taken into consideration when investigating potential icing on a UAM eVTOL aircraft. Another important note regarding UAM icing is the influence of the transition mechanism. Some UAM aircraft designs implement a vectored thrust configuration which allows some or all of the rotors to change the direction of the produced thrust. For the rotors, this would mean a transition from a rotational axis perpendicular to the flow direction to parallel, and vice versa. As mentioned in the earlier discussion, a change of flow direction may have implications on the ice accretion in glaze icing conditions. Therefore, an exhaustive study on UAM vehicle icing should include an icing investigation during the transition phase.

A phenomenon that is not considered in this paper is ice shedding, which is a common occurrence in rotating lifting surfaces due to high centrifugal forces. A detailed analysis regarding ice shedding would require information on the adhesion and cohesion forces acting on the airfoil surface and the ice [48]. In a theoretical scenario where the ice horns formed at −2 °C do not shed off the blade, it could hinder the rotor performance significantly, especially since the large rotor simulations were conducted under the assumption of vertical take-off

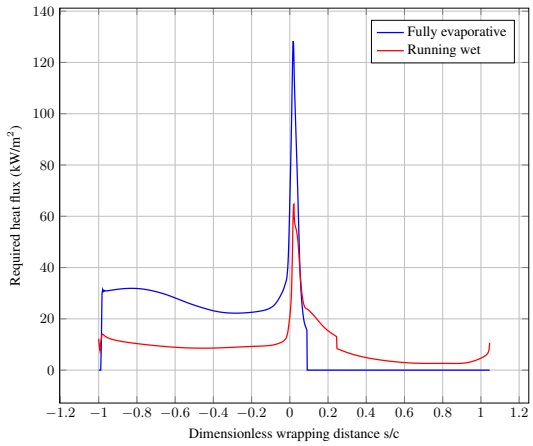

(a) 50% of the blade position.

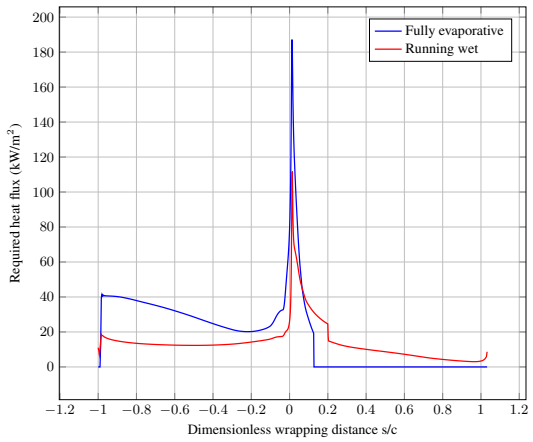

(b) 75% of the blade position.

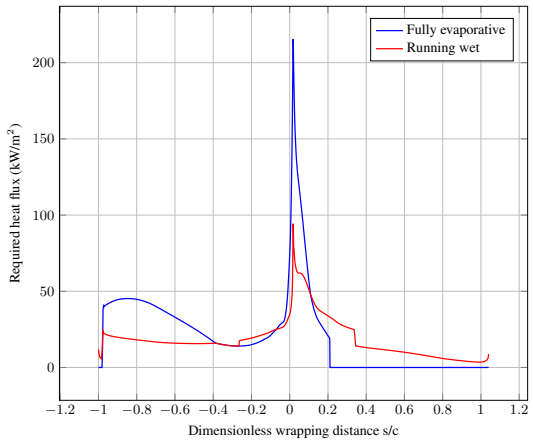

(c) 95% of the blade position.

Figure 20: Anti-icing load requirements for the 15-inch rotor sections in fully evaporative and running wet conditions at −15 °C.

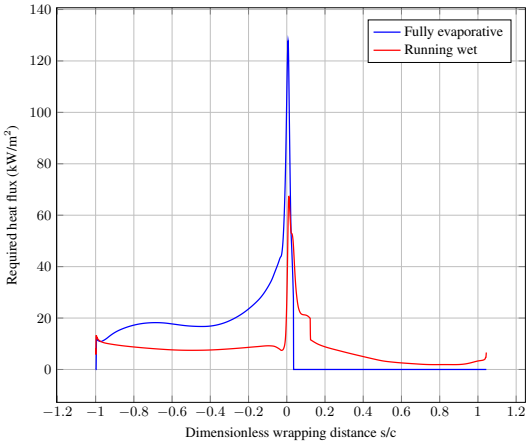

(a) 50% of the blade position.

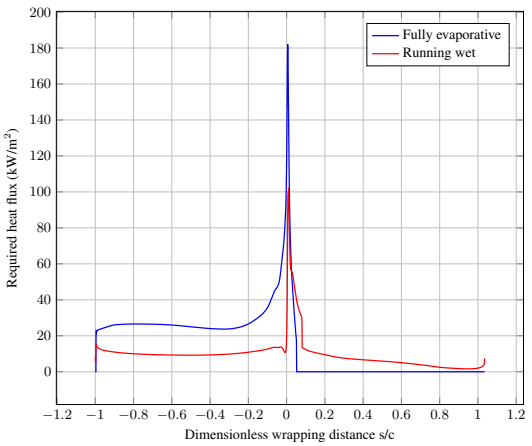

(b) 75% of the blade position.

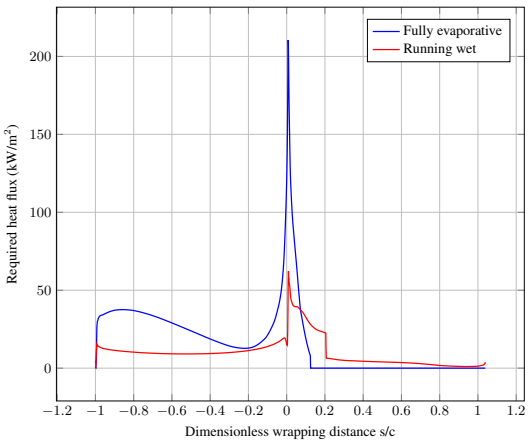

(c) 95% of the blade position.

Figure 21: Anti-icing load requirements for the 80-inch rotor sections in fully evaporative and running wet conditions at −15 °C.

and hover flight. It would be interesting to see how the large 80-inch rotor behaves in ambient temperatures close to the freezing point within an experimental framework to provide validation of these ice shape results.

Performance Degradation Simulation

The effect of icing on an eVTOL aircraft airfoil can be analyzed using the ice shape data and the roughness output file obtained from the ice accretion simulations. The airflow surrounding both clean and iced airfoils was calculated using FENSAP for a range of angles of attack. The study was done for a 15-inch and an 80-inch rotor and for two icing conditions to present a rime and a glaze icing condition. Icing in general serves as a hindrance to aerodynamic performance as it lowers the lift, increases the drag and changes the stall angle [3]. The performance simulation results show that the glaze icing condition experiences a stronger deterioration compared to the rime ice case. This could be addressed to the ice horns that typically form in glaze ice conditions for temperatures near the freezing point, while the ice accretion in very low temperatures tends to have a more streamlined shape. It can be seen, for example in Figure 14, that the ice horn led to a detachment of flow for the whole remaining airfoil chord length. This supports the observations made by Bragg et al. [12], stating that horn ice shapes have a significant negative influence on performance due to icing. It should also be noted, that the glaze ice simulation of the small rotor in this study was calculated with double the icing duration as the rime ice case, leading to larger ice accumulation and consequently, higher aerodynamic penalties.

Although horn and irregular ice shapes are key characteristics of a glaze ice type, the occasion when these shapes occur seems to differ depending on airfoil size, icing condition, and airflow direction. In a previous work by Müller and Hann [48], the studied propeller was observed to form ice horns at −10 °C and −15 °C. Whereas the small 15-inch rotor in this paper presents no horn ice at −5 °C nor in the lower temperatures. The geometries studied in both cases have a different size and rotational axis direction, though the LWC is similar with only a 0.03 g/m^3 difference. Previous studies show that the LWC values have an influence on the lift, drag, and moment [15]. The large 80-inch rotor displays an elongated ice horn at −5 °C and a small one on the upper side of the leading edge at −2 °C. These observations would suggest that determining the parameters that influence horn ice accretion, is equally vital to investigate performance degradation due to icing. Moreover, the stagnation point can not be predicted accurately, which might influence the ice horn angles and the ice accretion. Furthermore, the simulations in this paper were conducted under the assumption of a monodisperse droplet distribution, which assumes uniform droplet size. The droplet trajectory is influenced by its size since smaller droplets tend to follow the streamline while larger droplets have a more straight-lined flight path [10]. This lead to a higher collision rate with larger droplet sizes. Running an icing study with the Langmuir D distribution, as recommended by the FAA, would offer more realistic ice shapes and consequently more reliable performance data. However, the computational time costs would have to be taken into consideration.

Anti-icing Loads Simulation

Simulations were done to estimate the required anti-icing loads necessary to thermally mitigate the effects of ice. For an air temperature of −15 °C, the results show very high maximum heat flux requirements for both rotors. Anti-icing is the preferred IPS strategy for rotating lifting surfaces, due to their sensitivity toward aerodynamic penalties due to icing and ice shedding [3]. The power requirements of a fully evaporative system are almost doubled compared to those of a running wet system. However, with a running wet system there is a risk of runback icing, which could acquire due to the liquid water refreezing in areas without heating further down the chord [56]. Runback ice may occur in form of a spanwise-ridge shape, which could induce higher levels of aerodynamic penalties even compared to horn ice [12]. Ideally, the heating strips of a fully evaporative system are installed only at the impingement zone, whereas the heat pads in a running wet system should be installed on the blade surface area where water film exists [3]. However, this is not always the case as identifying these zones is a difficult task since they might shift depending on the flight condition. To increase power consumption efficiency, it should be looked into whether implementing both systems into one design is feasible. That way, the IPS mode can be activated depending on the oncoming icing condition. Running wet systems are more energy efficient at temperatures close to freezing point, due to the small temperature difference [3]. Whereas fully evaporative systems may be more suitable for lower temperatures as the area which requires heating is smaller [57].

Alternatively, it may be worthwhile to consider implementing the electrothermal ice protection system in combination with other IPS types, for example, a mechanical IPS type. The most common mechanical de-icing system is pneumatic boots, which are frequently used on the wings and propeller of light manned aircraft [3]. The pneumatic de-icing boots are a mature technology, lightweight and energy efficient [56]. However, the system is known to generate additional drag [58] and the efficiency is affected by large droplets, lower flight speeds, and surface roughness [59]. If the risks of pneumatic boots on an eVTOL rotor and the aircraft's tolerance to intercycle icing are well assessed, its use may be an option worth consideration aside from a fully electrothermal IPS. Although such hybrid systems could pose a challenge for smaller eVTOL drones due to their size, they may be feasible for larger eVTOL aircraft and may be worth consideration. Furthermore, to support the long-term goals of autonomous flights through eVTOL aircraft, an extensive study of icing in diverse meteorological conditions on various aircraft geometries is important for the IPS control systems design and development.

Uncertainties

Several assumptions were made to simplify the simulations presented in this manuscript. For example, the angle of attack in the 2D simulations. The angle of attack of a rotor is challenging to measure because it can change with the blade pitch angle, variation in local airspeed, location of the blade during rotation, blade flapping, and so on [50]. These aspects were not considered in the 2D simulations. Furthermore, 2D simulations are not capable of capturing the three-dimensional flow effects such as the blade root effect or the dynamic stall.

Compared to larger manned aircraft, there are fewer validation datasets available for aircraft in the lower Reynolds number regime. Müller and Hann [60] provide an extensive overview of available icing validation datasets. A good prediction of the flow transition from laminar to turbulent is important to calculate the energy balance during the icing process [61, 62]. In larger manned aviation, it is assumed that the existence of ice roughness can cause a flow transition to fully turbulent [12]. However, at a lower Reynolds number regime, the boundary layer thickness is larger and therefore, the fully-turbulent flow assumption may not be valid [21]. Furthermore, the simulations in this paper were only done on the rotors, while the influence of the rest of the aircraft structure is disregarded. This may have an impact on the forming ice shapes as the airflow approaching the rotors are no longer smooth and potentially disturbed by the aircraft structure or other rotors. Furthermore, several UAM eVTOL aircraft designs available utilize a form of vectored thrust. This means that some of the UAM eVTOL rotors are capable of shifting their rotation axis, and this was not regarded in the simulations done within this paper. Finally, ice-shedding events were not taken into consideration in this study. Centrifugal forces play a significant role in rotating lifting surfaces and can lead to ice shedding. Depending on the type of ice accretion [63], the air temperature [48], the icing duration, and the size of the rotor, the ice shedding effects should not be disregarded.

Summary

Within this paper, the effects of icing on eVTOL rotors using CFD simulations were investigated. Two rotors of different sizes were examined in this study. A small 15-inch rotor was chosen to represent eVTOL UAV drones, while a large 80-inch rotor was decided to illustrate the rotors used in UAM eVTOL aircraft. The ice accretion experiments were done on the small 15-inch rotor at −5 °C, −10 °C, and −15 °C with a wind velocity of 6 m/s and a rotational speed of 5000 RPM. The ice shapes were captured using the photogrammetry method. The CFD simulations in this paper were conducted using FENSAP-ICE from ANSYS. The turbulence is modeled using the one equation Spalart-Allmaras turbulence model. The simulations were done in a multishot set up, dividing the total icing time into 10 smaller steps, and the grid is remeshed between every step using Fluent Meshing. The simulation models were verified and validated against an experimental ice shape dataset of a scaled helicopter rotor blade with a NACA 0012 airfoil cross-section. Two cases were chosen to predict the ice shapes in rime and glaze icing conditions. Three meshes with varying refinement levels were generated to study the grid dependency.

The ice accretion experiments provide ice shapes with significant accretion around the leading edge of the airfoil for all cases, except at the tip region of the glaze icing condition at −5 °C. At 50% and 75% of the blade radius in − 5 °C air temperature, the ice shape shows ice horns forming at the leading edge. The largest ice accretion relative to the airfoil size is shown at an air temperature of − 10 °C and − 15 °C at the two outer sections of the blade, while the innermost section at 50% of the blade radius additionally displays ice at the upper part of the leading edge.

A total of 20 ice accretion simulations were performed for the two eVTOL rotors in various icing conditions. The temperatures range from −2 °C to −15 °C, while the LWC values vary between 0.319 – 0.595 g/m^3. The 2D ice accretion simulations were conducted on the blade cross-sections in the 50%, the 75%, and the 95% radial positions, while the 3D simulations were done on the whole rotor. The ice accretion simulation results agree with the observations of previous works regarding the influence of icing conditions, airfoil chord length, and rotational speed on ice accretion. Compared to a previous study on a UAV propeller, the small eVTOL rotor shows a more rime-like ice shape at −5 °C instead of a glaze ice characteristic. At −15 °C the ice shapes of both rotor and propeller display a typical rime ice shape. This could imply an influence of the rotational axis and airflow direction on the final ice shape in glaze ice conditions. The 2D ice shapes of the small eVTOL rotor in lower temperatures show similarities with the experimental ice shapes obtained from a test campaign in an icing wind tunnel, albeit with fewer details captured. This would suggest that a 2D ice accretion simulation is sufficient for the first assessment in cases where rime ice is expected. The rime ice accretion obtained through 3D simulation also displays a typical rime ice shape, albeit more streamlined, and the ice builds up more on the upper side of the airfoil leading edge. The ice shapes of the large 80-inch rotor blade sections display more variety of ice shapes and horns than the smaller 15-inch rotor, which could indicate a higher sensitivity to icing parameter changes. At −15 °C, the predicted ice shape has a typical rime ice shape with the largest accumulation with regards to airfoil size being at the outer section of the blade. At temperatures near the freezing point, the 80-inch rotor sections demonstrate highly irregular ice shapes with horns. The ice accretion at −5 °C presents the most ice mass and a large horn at the leading edge. The ice horns formed at 50% of the blade radius section for −2 °C are shown to cause large flow disruption aft of the ice, but there is no ice predicted for the middle and outer sections. The 3D simulation of the 80-inch rotor at −15 °C display less ice accretion on the inner sections and no ice at all for the outer region of the blade. This may be caused by the higher stagnation temperature at the tip region of the rotor, which can increase the local temperature significantly and prevent ice from accumulating. This behavior has also been observed in larger manned aviation vehicles [17]. This may suggest, that a UAM eVTOL rotor behaves more like the rotor of a larger manned aircraft than that of a UAV.

For the performance degradation simulations, the lift and drag coefficients of the clean and iced airfoils were calculated for a range of angles of attacks and compared. The results show that the iced airfoil with glaze and horn ice shapes go through a larger performance loss compared to the airfoils with a rime ice shape. It is also observed, that the circumstances in which horn ice develops depend not only on the air temperature but also on airfoil size, droplet parameter, and airflow direction. This would indicate that determining the parameters inducing horn ice accretion is required to be able to predict the performance loss due to icing. Finally, the anti-icing loads required for designing an electrothermal ice protection system were calculated. At an air temperature of −15 °C, the small 15-inch rotor requires a maximum of 180 kW/m^2 of power to evaporate the impinging water droplets, while the large 80-inch rotor needs 170 kW/m^2. The power requirements for a running wet condition are lower, but the risks of runback ice are higher. To lower the IPS power consumption, implementing both anti-icing strategies for different conditions may be looked into. It may also be worthwhile to look into other IPS strategies aside from electrothermal, especially for the larger rotor. In general, there is a need to obtain knowledge regarding the severity of ice in various icing conditions on different aircraft geometries to develop an IPS control system with autonomous capabilities.

To conclude, the results in this paper show that ice accumulates faster for the small rotor cases. However, the ice shapes present fewer ice horns even in conditions that are typical of glaze icing conditions. The large rotor presents less ice accretion in comparison. However, the ice that does build up tends to grow irregularly and is more prone to ice horn formations, which can cause significant aerodynamic penalties. Furthermore, should the UAM aircraft possess thrust vectoring capabilities, its transition mechanism should be taken into account when investigating the effects of icing. As the behavior of both rotors is different, this would indicate that the small and the large eVTOL rotors would require different ice mitigation strategies. A good understanding of the ice accretion of the rotor in different icing conditions is essential to investigate the aerodynamic effects of icing on an eVTOL aerial vehicle. Considering the variety of ice shapes obtained in temperatures close to the freezing point and the performance degradation caused, it would be beneficial to conduct future studies for this temperature range. Obtaining additional experimental data would also be an interest as it can validate the simulation results.

Acknowledgements

The numerical simulations were performed on resources provided by the National Infrastructure for High Performance Computing and Data Storage in Norway (UNINETT Sigma2) on the Fram supercomputer, under project code NN9613K Notur/NorStore. The author would also like to the ERASMUS+ program for the financial aid awarded to support this work which was done as part of a master's thesis.

Contact Information

Henidya Heramarwan (she/her)
st111026@stud.uni-stuttgart.de / henidyah@stud.ntnu.no

References

1. *Advanced Air Mobility and Urban Air Mobility | Federal Aviation Administration* `https://www.faa.gov/uas/advanced_operations/urban_air_mobility` (2022).

2. Hill, B. P. *et al. UAM Vision Concept of Operations (ConOps) UAM Maturity Level (UML) 4* NTRS Author Affiliations: Deloitte (United States), Langley Research Center, National Aeronautics and Space Administration NTRS Document ID: 20205011091 NTRS Research Center: Headquarters (HQ) (Dec. 2, 2020). https://ntrs.nasa.gov/citations/20205011091 (2022).
3. Hann, R. & Johansen, T. *Unsettled Topics in Unmanned Aerial Vehicle Icing* (SAE International, Apr. 27, 2020). https://saemobilus.sae.org/content/EPR2020008/ (2022).
4. *Urban Air Mobility: Targeting autonomous flight operations from the beginning* Roland Berger. Last Modified: 2021-08-26T14:15+02:00. https://www.rolandberger.com/en/Insights/Publications/Urban-Air-Mobility-Targeting-autonomous-flight-operations-from-the-beginning.html (2023).
5. Goyal, R. *et al. Urban Air Mobility (UAM) Market Study - Booz Allen Hamilton Technical Briefing* NTRS Author Affiliations: Booz Allen Hamilton (United States), University of California, Berkeley NTRS Report/Patent Number: HQ-E-DAA-TN64105 NTRS Document ID: 20190000517 NTRS Research Center: Headquarters (HQ). https://ntrs.nasa.gov/citations/20190000517 (2022).
6. *14 CFR Appendix C to Part 25 - Appendix C to Part 25* LII / Legal Information Institute. https://www.law.cornell.edu/cfr/text/14/appendix-C_to_part_25 (2023).
7. Bernstein, B. C., Wolff, C. A. & McDonough, F. An Inferred Climatology of Icing Conditions Aloft, Including Supercooled Large Drops. Part I: Canada and the Continental United States. *Journal of Applied Meteorology and Climatology* **46,** 1857–1878. ISSN: 1558-8432, 1558-8424. https://journals.ametsoc.org/doi/10.1175/2007JAMC1607.1 (2022) (Nov. 1, 2007).
8. Bernstein, B. C. & Le Bot, C. An Inferred Climatology of Icing Conditions Aloft, Including Supercooled Large Drops. Part II: Europe, Asia, and the Globe. *Journal of Applied Meteorology and Climatology* **48,** 1503–1526. ISSN: 1558-8432, 1558-8424. http://journals.ametsoc.org/doi/10.1175/2009JAMC2073.1 (2022) (Aug. 1, 2009).
9. *AC 91-74B - Pilot Guide: Flight in Icing Conditions* https://www.faa.gov/documentlibrary/media/advisory_circular/ac_91-74b.pdf.
10. Battisti, L. *Wind Turbines in Cold Climates: Icing Impacts and Mitigation Systems* Google-Books-ID: GTi2BgAAQBAJ. 355 pp. ISBN: 978-3-319-05191-8 (Springer, Feb. 16, 2015).
11. Hann, R. & Johansen, T. A. UAV Icing: The Influence of Airspeed and Chord Length on Performance Degradation. *Aircraft Engineering and Aerospace Technology* **93,** 832–841. ISSN: 1748-8842, 1748-8842. https://www.emerald.com/insight/content/doi/10.1108/AEAT-06-2020-0127/full/html (2022) (Aug. 5, 2021).
12. Bragg, M., Broeren, A. & Blumenthal, L. Iced-Airfoil Aerodynamics. *Progress in Aerospace Sciences* **41,** 323–362. ISSN: 03760421. https://linkinghub.elsevier.com/retrieve/pii/S0376042105000801 (2022) (July 2005).
13. Janjua, Z. A., Turnbull, B., Hibberd, S. & Choi, K.-S. Mixed ice accretion on aircraft wings. *Physics of Fluids* **30,** 027101. ISSN: 1070-6631, 1089-7666. http://aip.scitation.org/doi/10.1063/1.5007301 (2023) (Feb. 2018).
14. Kind, R. J., Potapczuk, M. G., Feo, A., Golia, C. & Shah, A. D. Experimental and computational simulation of in-flight icing phenomena. *Progress in Aerospace Sciences* **34,** 257–345. ISSN: 0376-0421. https://www.sciencedirect.com/science/article/pii/S0376042198800018 (2023) (July 1, 1998).
15. Fajt, N., Hann, R. & Lutz, T. The Influence of Meteorological Conditions on the Icing Performance Penalties on a UAV Airfoil (2019).
16. Lynch, F. T. & Khodadoust, A. Effects of ice accretions on aircraft aerodynamics. *Progress in Aerospace Sciences* **37,** 669–767. ISSN: 0376-0421. https://www.sciencedirect.com/science/article/pii/S0376042101000185 (2023) (Nov. 1, 2001).
17. Gent, R. W., Dart, N. P. & Cansdale, J. T. Aircraft icing. *Philosophical Transactions of the Royal Society of London. Series A: Mathematical, Physical and Engineering Sciences* **358** (ed Poots, G.) 2873–2911. ISSN: 1364-503X, 1471-2962. https://royalsocietypublishing.org/doi/10.1098/rsta.2000.0689 (2022) (Nov. 15, 2000).
18. Flemming, R. *The past twenty years of icing research and development at Sikorsky Aircraft* in *40th AIAA Aerospace Sciences Meeting & Exhibit* 40th AIAA Aerospace Sciences Meeting & Exhibit (American Institute of Aeronautics and Astronautics, Reno,NV,U.S.A., Jan. 14, 2002). https://arc.aiaa.org/doi/10.2514/6.2002-238 (2023).
19. Hann, R. & Wallisch, J. *UAV Database* in collab. with Hann, R. & Technology, N. U. O. S. bibinitperiod. Type: dataset. 2020. https://dataverse.no/citation?persistentId=doi:10.18710/L41IGQ (2023).
20. Szilder, K. & McIlwain, S. *In-Flight Icing of UAVs - The Influence of Reynolds Number on the Ice Accretion Process* in. Aerospace Technology Conference and Exposition (Oct. 18, 2011), 2011–01–2572. https://www.sae.org/content/2011-01-2572/ (2022).
21. Hann, R. *UAV Icing: Challenges for computational fluid dynamic (CFD) tools* in. International Conference on Computational Fluid Dynamics (Maui, USA, July 2022).
22. Williams, N., Benmeddour, A., Brian, G. & Ol, M. *The effect of icing on small unmanned aircraft low Reynolds number airfoils* in *17th Australian International Aerospace Congress : AIAC 2017* ISSN: 9781922107855 (), 19–25. https://search.informit.org/doi/abs/10.3316/informit.738050435297237 (2023).
23. Müller, N., Hann, R. & Lutz, T. *UAV Icing: Numerical Simulation of Propeller Ice Accretion* in *AIAA AVIATION 2021 FORUM* AIAA AVIATION 2021 FORUM (American Institute of Aeronautics and Astronautics, VIRTUAL EVENT, Aug. 2, 2021). ISBN: 978-1-62410-610-1. https://arc.aiaa.org/doi/10.2514/6.2021-2673 (2022).
24. Liu, Y., Li, L., Chen, W., Tian, W. & Hu, H. An experimental study on the aerodynamic performance degradation of a UAS propeller model induced by ice accretion process. *Experimental Thermal and Fluid Science* **102,** 101–112. ISSN: 0894-1777. https://www.sciencedirect.com/science/article/pii/S0894177718314882 (2022) (Apr. 1, 2019).
25. Yan, S., Opazo, T. I., Langelaan, J. W. & Palacios, J. L. Experimental Evaluation and Flight Simulation of Coaxial-Rotor Vehicles in Icing Clouds. *Journal of the American Helicopter Society* **65,** 1–15 (Apr. 1, 2020).
26. Scavuzzo, R., Chu, M. & Ananthaswamy, V. *Influence of Aerodynamic Forces in Ice Shedding* in *29th Aerospace Sciences Meeting* 29th Aerospace Sciences Meeting (American Institute of Aeronautics and Astronautics, Reno,NV,U.S.A., Jan. 7, 1991). https://arc.aiaa.org/doi/10.2514/6.1991-664 (2023).

27. Tiihonen, M., Jokela, T., Makkonen, L. & Bluemink, G.-J. VTT Icing wind tunnel 2.0: Winterwind International Wind Energy Conference. *Winterwind Presentations 2016.* https://winterwind.se/presentations-2016/ (2022) (Feb. 10, 2016).

28. Robotics, T. *Series 1580 Test Stand* Tyto Robotics. https://www.tytorobotics.com/products/series-1580-test-stand-bundle (2022).

29. *Ansys FENSAP-ICE | In-Flight Aircraft Icing Simulation* https://www.ansys.com/products/fluids/ansys-fensap-ice (2023).

30. Morency, F., Beaugendre, H., Baruzzi, G. & Habashi, W. *FENSAP-ICE - A comprehensive 3D simulation system for in-flight icing* in *15th AIAA Computational Fluid Dynamics Conference* 15th AIAA Computational Fluid Dynamics Conference (American Institute of Aeronautics and Astronautics, Anaheim,CA,U.S.A., June 11, 2001). https://arc.aiaa.org/doi/10.2514/6.2001-2566 (2023).

31. Ozcer, I., Switchenko, D., Baruzzi, G. S. & Chen, J. *Multi-Shot Icing Simulations with Automatic Re-Meshing* in. International Conference on Icing of Aircraft, Engines, and Structures (June 10, 2019), 2019–01–1956. https://www.sae.org/content/2019-01-1956/ (2022).

32. Bourgault, Y., Boutanios, Z. & Habashi, W. G. Three-Dimensional Eulerian Approach to Droplet Impingement Simulation Using FENSAP-ICE, Part 1: Model, Algorithm, and Validation. *Journal of Aircraft* **37.** Publisher: American Institute of Aeronautics and Astronautics _eprint: https://doi.org/10.2514/2.2566, 95–103. ISSN: 0021-8669. https://doi.org/10.2514/2.2566 (2023) (2000).

33. *ANSYS FENSAP-ICE User Manual* Jan. 2021.

34. Craggs, J. D. The Collected Works of Irving Langmuir. *Physics Bulletin* **13,** 86–87. ISSN: 0031-9112. https://iopscience.iop.org/article/10.1088/0031-9112/13/3/011 (2023) (Mar. 1962).

35. Beaugendre, H., Morency, F. & Habashi, W. G. FENSAP-ICE's Three-Dimensional In-Flight Ice Accretion Module: ICE3D. *Journal of Aircraft* **40.** Publisher: American Institute of Aeronautics and Astronautics _eprint: https://doi.org/10.2514/2.3113, 239–247. ISSN: 0021-8669. https://doi.org/10.2514/2.3113 (2023) (2003).

36. Bourgault, Y., Beaugendre, H. & Habashi, W. G. Development of a Shallow-Water Icing Model in FENSAP-ICE. *Journal of Aircraft* **37.** Publisher: American Institute of Aeronautics and Astronautics _eprint: https://doi.org/10.2514/2.2646, 640–646. ISSN: 0021-8669. https://doi.org/10.2514/2.2646 (2023) (2000).

37. Messinger, B. Equilibrium Temperature of an Unheated Icing Surface as a Function of Air Speed. *Journal of the Aeronautical Sciences* **20.** Publisher: American Institute of Aeronautics and Astronautics _eprint: https://doi.org/10.2514/8.2520, 29–42. https://doi.org/10.2514/8.2520 (2023) (1953).

38. Han, Y., Palacios, J. L. & Smith, E. C. *An Experimental Correlation between Rotor Test and Wind Tunnel Ice Shapes on NACA 0012 Airfoils* in. SAE 2011 International Conference on Aircraft and Engine Icing and Ground Deicing (June 13, 2011), 2011–38–0092. https://www.sae.org/content/2011-38-0092/ (2022).

39. *Mejzlik.eu - Design and manufacturing top-quality propellers* https://www.mejzlik.eu/ (2023).

40. Selig, M. *UIUC airfoil data site* https://search.library.wisc.edu/catalog/999919007002121 (Urbana, Ill. : Department of Aeronautical and Astronautical Engineering University of Illinois at Urbana-Champaign, 1996-, 1996).

41. *NX | Siemens Software* Siemens Digital Industries Software. https://www.plm.automation.siemens.com/global/en/products/nx/ (2023).

42. *Fidelity Pointwise* https://www.cadence.com/en_US/home/tools/system-analysis/computational-fluid-dynamics/pointwise.html (2023).

43. *Unstructured Domains, T-Rex Tab* https://www.pointwise.com/user-manual/grid/solve/unstructured-domains/t-rex.html (2023).

44. Drela, M. *XFOIL: An Analysis and Design System for Low Reynolds Number Airfoils* in *Low Reynolds Number Aerodynamics* (ed Mueller, T. J.) (Springer, Berlin, Heidelberg, 1989), 1–12. ISBN: 978-3-642-84010-4.

45. *Examining Spatial (Grid) Convergence* https://www.grc.nasa.gov/WWW/wind/valid/tutorial/spatconv.html (2022).

46. Richardson, L. The approximate arithmetical solution by finite differences of physical problems involving differential equations, with an application to the stresses in a masonry dam. *Philosophical Transactions of the Royal Society of London. Series A, Containing Papers of a Mathematical or Physical Character* **210,** 307–357. ISSN: 0264-3952, 2053-9258. https://royalsocietypublishing.org/doi/10.1098/rsta.1911.0009 (2023) (Jan. 1911).

47. Richardson, L. & Gaunt, J. The deferred approach to the limit. *Philosophical Transactions of the Royal Society of London. Series A, Containing Papers of a Mathematical or Physical Character* **226,** 299–361. ISSN: 0264-3952, 2053-9258. https://royalsocietypublishing.org/doi/10.1098/rsta.1927.0008 (2023) (Jan. 1927).

48. Müller, N. C. & Hann, R. *UAV Icing: A Performance Model for a UAV Propeller in Icing Conditions* in *AIAA AVIATION 2022 Forum* AIAA AVIATION 2022 Forum (American Institute of Aeronautics and Astronautics, Chicago, IL & Virtual, June 27, 2022). ISBN: 978-1-62410-635-4. https://arc.aiaa.org/doi/10.2514/6.2022-3903 (2022).

49. World Meteorological Organization. Commission for Maritime Meteorology. *The Beaufort scale of wind force : (technical and operational aspects)* https://search.library.wisc.edu/catalog/999768644902121 (Geneva : WMO, 1970., 1970).

50. *Helicopter Flying Handbook* https://www.faa.gov/regulations_policies/handbooks_manuals/aviation/helicopter_flying_handbook (United States Department of Transportation, Federal Aviation Administration, 2019).

51. Shen, W. Z., Hansen, M. O. L. & Sørensen, J. N. Determination of the angle of attack on rotor blades. *Wind Energy* **12.** _eprint: https://onlinelibrary.wiley.com/doi/pdf/10.1002/we.277, 91–98. ISSN: 1099-1824. https://onlinelibrary.wiley.com/doi/abs/10.1002/we.277 (2023) (2009).

52. Roache, P. J. *Verification and Validation in Computational Science and Engineering* 446 pp. ISBN: 978-0-913478-08-0 (Hermosapublishers, Albuquerque, N.M, 1998).

53. Anderson, J. D. *Fundamentals of Aerodynamics* Sixth edition. 1130 pp. ISBN: 978-1-259-12991-9 (McGraw Hill Education, New York, NY, 2017).

54. Hann, R., Hearst, R. J., Sætran, L. R. & Bracchi, T. Experimental and Numerical Icing Penalties of an S826 Airfoil at Low Reynolds Numbers. *Aerospace* **7.** Number: 4 Publisher: Multidisciplinary Digital Publishing Institute, 46. ISSN: 2226-4310. https://www.mdpi.com/2226-4310/7/4/46 (2022) (Apr. 2020).

55. Hann, R. *Atmospheric Ice Accretions, Aerodynamic Icing Penalties, and Ice Protection Systems on Unmanned Aerial Vehicles* Doctoral Thesis (Norwegian University of Science and Technology, Trondheim, Norway, July 2020). https://ntnuopen.ntnu.no/ntnu-xmlui/handle/11250/2657638.

56. Thomas, S. K., Cassoni, R. P. & MacArthur, C. D. Aircraft anti-icing and de-icing techniques and modeling. *Journal of Aircraft* **33,** 841–854. ISSN: 0021-8669, 1533-3868. https://arc.aiaa.org/doi/10.2514/3.47027 (2023) (Sept. 1996).

57. Hann, R. *UAV Icing: Comparison of LEWICE and FENSAP-ICE for Anti-Icing Loads* in *AIAA Scitech 2019 Forum* AIAA Scitech 2019 Forum (American Institute of Aeronautics and Astronautics, San Diego, California, Jan. 7, 2019). ISBN: 978-1-62410-578-4. https://arc.aiaa.org/doi/10.2514/6.2019-1286 (2023).

58. Albright, A. E., Kohlman, D. L., Schweikhard, W. G. & Evanich, P. *Evaluation of a pneumatic boot deicing system on a general aviation wing model* KU-FRL-464-2. NTRS Author Affiliations: Kansas Univ., NASA Lewis Research Center NTRS Document ID: 19810016530 NTRS Research Center: Legacy CDMS (CDMS) (June 1, 1981). https://ntrs.nasa.gov/citations/19810016530 (2023).

59. Pellicano, P. & Riley, J. *Residual and Inter-cycle Ice for Lower-Speed Aircraft with Pneumatic Boots* in *45th AIAA Aerospace Sciences Meeting and Exhibit* 45th AIAA Aerospace Sciences Meeting and Exhibit (American Institute of Aeronautics and Astronautics, Reno, Nevada, Jan. 8, 2007). ISBN: 978-1-62410-012-3. https://arc.aiaa.org/doi/10.2514/6.2007-1090 (2023).

60. Hann, R. & Müller, N. *Icing Validation Database* in collab. with Hann, R. & Technology, N. U. O. S. bibinitperiod. Type: dataset. 2020. https://dataverse.no/citation?persistentId=doi:10.18710/5XYALW (2022).

61. Liu, Y. & Hu, H. *An Experimental Investigation on the Convective Heat Transfer Process over an Ice Roughened Airfoil* in *54th AIAA Aerospace Sciences Meeting* 54th AIAA Aerospace Sciences Meeting (American Institute of Aeronautics and Astronautics, San Diego, California, USA, Jan. 4, 2016). ISBN: 978-1-62410-393-3. https://arc.aiaa.org/doi/10.2514/6.2016-1978 (2023).

62. Ignatowicz, K., Morency, F. & Beaugendre, H. Sensitivity Study of Ice Accretion Simulation to Roughness Thermal Correction Model. *Aerospace* **8,** 84. ISSN: 2226-4310. https://www.mdpi.com/2226-4310/8/3/84 (2023) (Mar. 19, 2021).

63. Pellicano, P., Dumont, C., Smith, T. & Riley, J. *Propeller Icing Tunnel Test on a Full-Scale Turboprop Engine* Data Report DOT/FAA/AR-06/60 (FAA, Mar. 2010).